2. GLOBAL CLIMATE—P. W. Thorne, Ed.

a. *Summary*—P. W. Thorne

2008 was cool, but only in the context of the last few very warm years. It still ranks within the 10 warmest years on record. The primary cause was a moderate to strong La Niña event. 1999, the last year with a similarly large La Niña, was 0.1°C colder. Surface cooling straddled 2007/08. Because the tropospheric response lags the surface, 2008 ranked outside the top 10 warmest tropospheric years regardless of choice of dataset. This difference in rankings does not reflect, as has been variously posited, a fundamental issue for surface record homogeneity.

This year's global chapter incorporates many more climate variables than previous vintages. Where possible, anomalies for those variables in Plate 2.1 and in the individual section diagrams have been plotted in a consistent format to aid comparisons. We have also used more independently derived datasets. The spread provides guidance on how well we can characterize the climate system's evolution. There are substantial questions about how well we understand, particularly, the long-term trends in many variables. However, it is clear that over the 30-yr period of truly global monitoring from satellites, the world has overall become warmer, moister, and probably stormier.

Plate 2.1 shows that the dominant factor for almost all climate variables in 2008 was the La Niña event. total column water vapor, cloud cover, and precipitation provide a consistent picture of areas of drying and moistening typical of a La Niña. The sea level pressure signature of La Niña is also readily apparent, as are the surface and tropospheric temperature signals. Northern Hemispheric snow cover extent for the year was well below average despite record maximum coverage in January. Top-of-atmosphere radiation data imply that 2008 saw a net receipt of radiation into the climate system, but further work on these data is required so this should be treated as provisional. Greenhouse gas concentrations continued to rise, with CO_2 increasing by more than expected based on the 1979 to 2007 trend. Ozone-depleting gas concentrations continued to fall. Total-column ozone concentrations remained well below pre-1980 levels, and the Antarctic ozone hole was particularly large and long-lived. Limited preliminary data imply that in 2008 glaciers continued to lose mass, and full data for 2007 show it was the 17th consecutive year of loss. New land-use and vegetation-state products highlight how we are both directly and indirectly systematically altering the land-surface characteristics. Datasets used in this chapter that are publicly available are referenced in Table 2.5 at the chapter's end.

b. *Temperatures*

1) Global surface temperatures in 2008—M. J. Menne and J. J. Kennedy

2008 was the coolest year since 2000, but still within the 10 warmest on record according to all three datasets [GISS, Hansen et al. 2001; HadCRUT3, Brohan et al. 2006; NCDC, Smith and Reynolds 2005]. Each analysis is based on air temperature data over land and sea-surface temperatures observed from ships and buoys (and satellites in the case of NCDC and GISS) with adjustments to account for changes in observing system bias. Differences in techniques

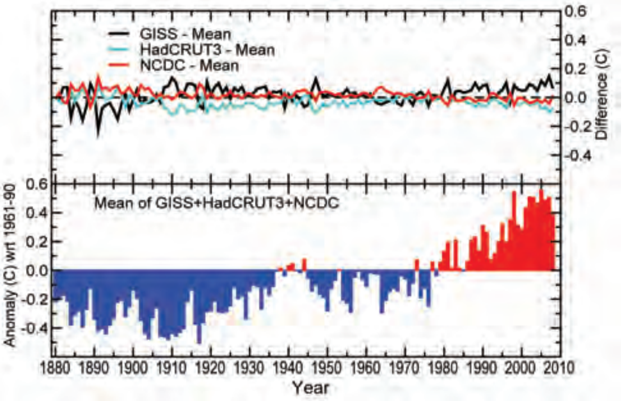

Fig. 2.1. Global surface temperature anomalies with respect to the 1961 to 1990 average. (bottom) Mean of GISS, HadCRUT3 and NCDC; upper panel: difference between GISS, HadCRUT3, NCDC and the mean.

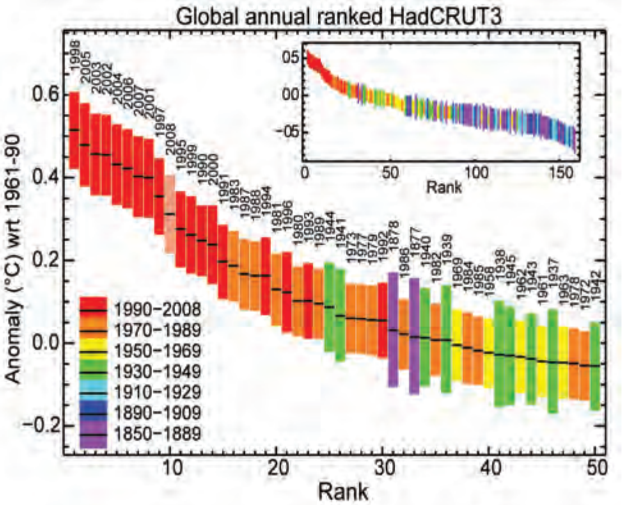

Fig. 2.2. Year-by-year temperature rankings and 95% confidence limits for the HadCRUT3 temperature analysis. The main panel shows the 50 warmest years and the inset shows the full 159-yr record.

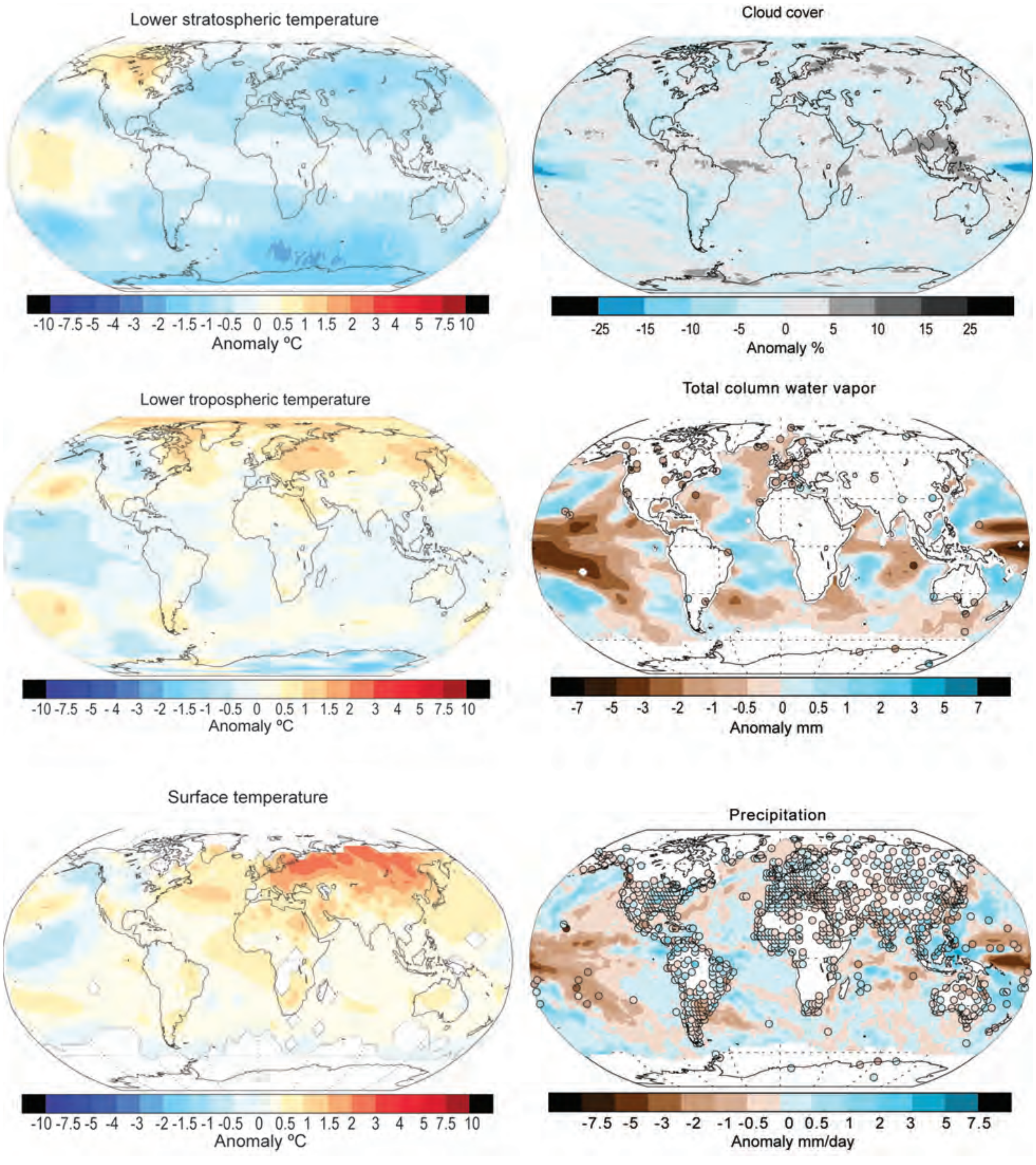

lead to differences in detail especially in regions with sparse data and in the specifics of yearly rankings. However, they are in strong agreement regarding the low-frequency variations in the surface temperature signal (Fig. 2.1, top). Differences rarely exceed 0.1°C and are much smaller than the increase in global mean temperature since the 1970s. Moreover, the uncertainties imply that 2008 is effectively indistinguishable from several of the other high-ranking years (Fig. 2.2). Notably, the 20 warmest years have all occurred since 1981, and the 10 warmest have all occurred in the past 12 years.

2008 was cooler than recent years in part because of the moderate to strong La Niña that developed in the latter half of 2007. La Niña peaked in early 2008 as indicated by the negative anomalies at equatorial latitudes (Fig. 2.3). Evidence of the impact of the ENSO cycle on tropical temperatures can be seen

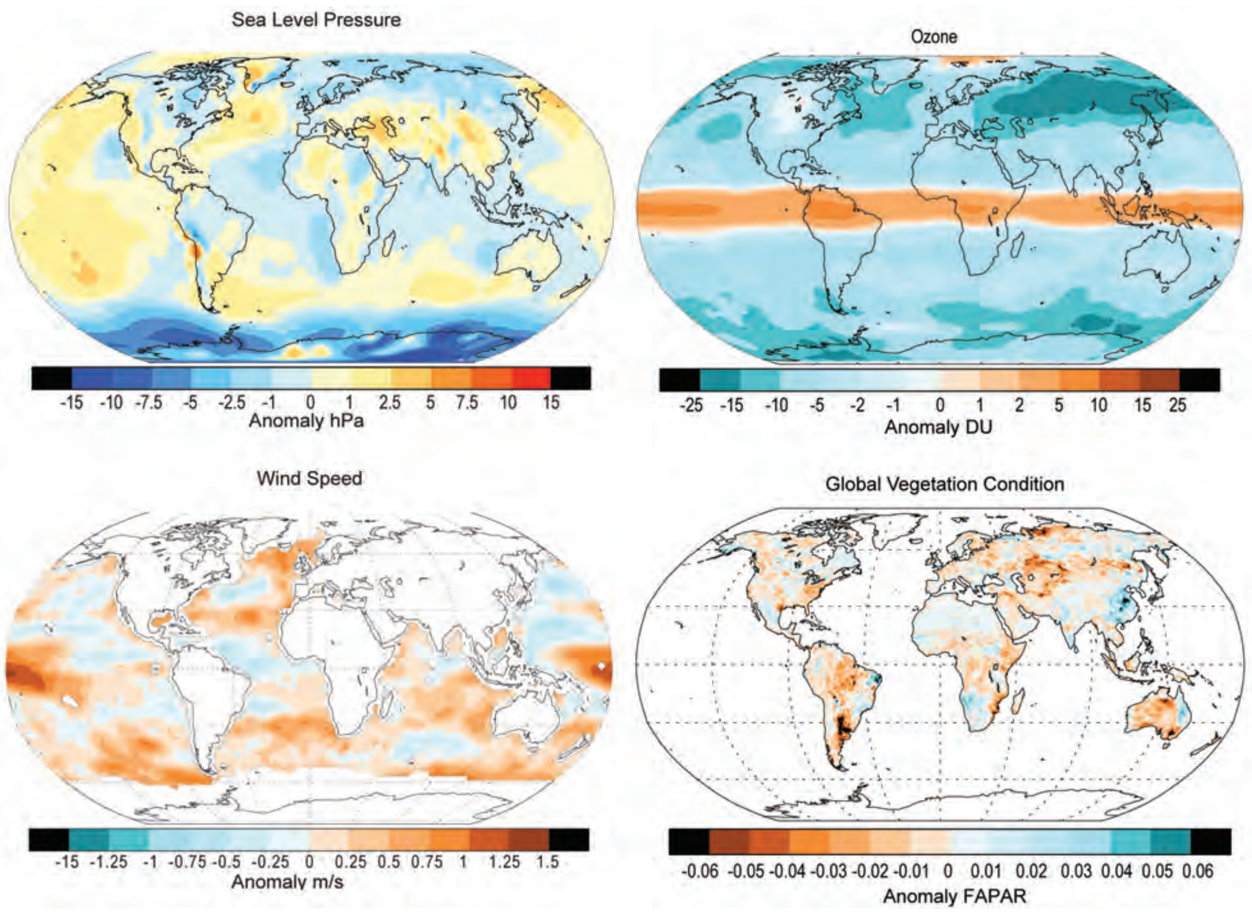

Plate 2.1. Global annual anomaly maps for those variables for which it was possible to create a meaningful anomaly estimate. Climatologies differ among variables, but spatial patterns should largely dominate over choices of climatology period. Dataset sources and climatologies are given in the form (dataset name/data source, start year–end year) for each variable. See relevant section text and figures for more details. Lower stratospheric temperature (RSS MSU 1981–90); lower tropospheric temperature (UAH MSU 1981–90); surface temperature (NCDC 1961–90); cloud cover (PATMOS-x 1982–2008); total column water vapor (SSM/I/GPS 1997–2008); precipitation (RSS/GHCN 1989–2008); mean sea level pressure (HadSLP2r 1961–90); wind speed (SSM/I 1988–2007); total column ozone (annual mean global total ozone anomaly for 2008 from SCIAMACHY. The annual mean anomalies were calculated from 1° × 1.25° gridded monthly data after removing the seasonal mean calculated from GOME (1996–2003) and SCIAMACHY (2003–07)]; vegetation condition [annual FAPAR anomalies relative to Jan 1998 to Dec 2008 from monthly FAPAR products at 0.5° × 0.5° [derived from SeaWiFS (NASA) and MERIS (ESA) data].

throughout the record. Figure 2.3 also illustrates the increase in temperatures at high latitudes of the Northern Hemisphere in recent decades. As shown in Plate 2.1, panel 3, this trend continued into 2008 when above-average temperatures were recorded across all of northern Eurasia and much of the Arctic.

2) Lower tropospheric temperatures—J. Christy, D. Seidel, C. Mears, and L. Haimberger

The 2008 global average temperature of the lower tropospheric layer (TLT, surface to ~8km) was cooler than in recent years due to the La Niña. When the surface cools, the troposphere responds with similar temperature changes, which for the global average lag the surface fluctuations by 2 to 4 months (Christy and McNider 1994). The surface was coolest in January 2008, and consequently the troposphere was coolest in May (~0.4°K below the 2007 average). Overall, 2008 was cooler than 2007 by about 0.25°K. The 51-yr time series of globally averaged TLT (Fig. 2.4) indicate this recent dip. 2008 was the 15th warmest of the mean of the datasets (individual rankings by dataset: 12th to 18th).

Datasets in Fig. 2.4 were constructed by different teams using either balloon-based radiosondes or satellite-based microwave sensors. Continuing

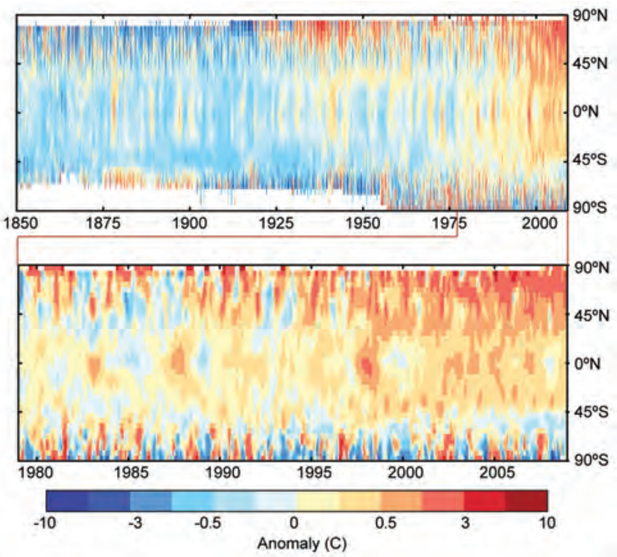

Fig. 2.3. HadCRUT3 monthly average temperature anomalies by latitude for the period 1850 to 2008. The data have been smoothed in space and time using a 1:2:1 filter. White areas indicate missing data.

research has developed procedures to account for inhomogeneities in these systems to provide the most confident estimates of the temperature evolution. Reanalyses have the potential to provide a physically consistent synthesis of all data sources, but inhomogeneities in their data inputs and the intrusion of model biases give reason to discount current reanalysis-based trends (e.g., Karl et al. 2006, Sakamoto and Christy 2009).

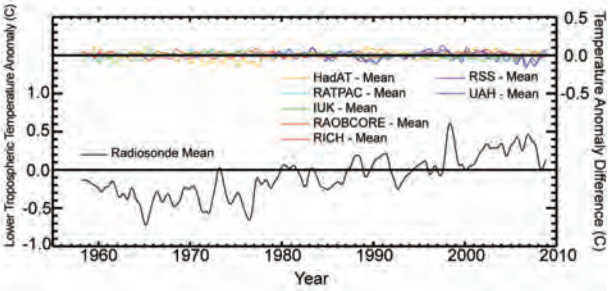

Fig. 2.4. Global mean lower tropospheric temperature (1958–2008) from multiple datasets, including five radiosonde datasets (HadAT, IUK, RAOBCORE, RATPAC, and RICH) and two satellite MSU datasets (RSS, UAH). All time series are for the layer sampled by MSU retrieval 2LT, spanning 0–8 km in altitude. Black curve is the average of all available radiosonde datasets, and the colored curves show differences between individual datasets and this average. References for the radiosonde datasets are Thorne et al. 2005b, Sherwood et al. 2008, Haimberger 2007, Free et al. 2005, and Haimberger et al. 2008; and for the MSU datasets are Mears and Wentz 2009a and Christy et al. 2003.

The La Niña signal of the cool tropics is clear in the first half of 2008 (Fig. 2.5). Similar but longer-lived cool tropical events occurred around 1985, 1989, and 2000. The cooling in 1992 is related to the volcanic eruption of Mt. Pinatubo. During the last decade or so there has been a general shift to warmer temperatures in the northern latitudes and tropics.

The estimated trend for both the entire time series beginning in 1958 (radiosonde era) and since 1979 (satellite era) is +0.145 ±0.02°C decade^{-1} with the range of the trends calculated from the various datasets. There is no indication of acceleration of the trend, though the relatively large excursions from the trend line make possible other interpretations than a simple trend. Decadal variations and shifts tend to limit the meaning of linear trend estimates (Seidel and Lanzante 2004).

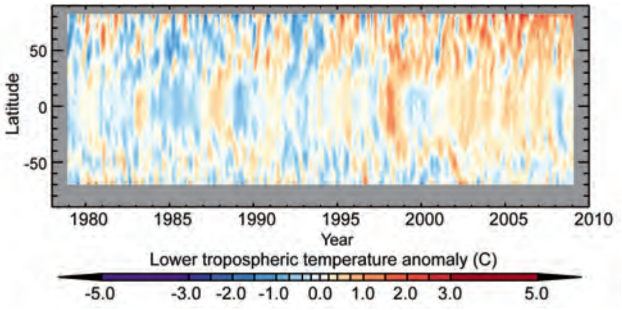

Fig. 2.5. Zonal mean lower tropospheric temperature anomalies (1979–2008) with respect to the 1979–88 mean. Anomalies based on MSU Channel 2LT data, as processed by RSS (Mears and Wentz 2009a).

The atmosphere responded to the equatorial Pacific influence in 2008 in a common "teleconnection" pattern (Plate 2.1, panel 2) with cold equatorial Pacific anomalies, warm regions in the north and south Pacific, and cold regions farther east of these, including into North America (Wallace et al. 2005). Other regions of warm anomalies in 2008 include Arctic Canada and most of Russia. Aside from the broad, cool anomalies in the tropics, the Southern Hemisphere was mostly below average.

3) Stratospheric temperatures—D. Seidel, J. Christy, and C. Mears

The 2008 annual average temperature of the lower stratosphere was similar to that of the last dozen years (Fig. 2.6). Globally, the lower stratosphere has been about 1.5°C cooler over the past decade than

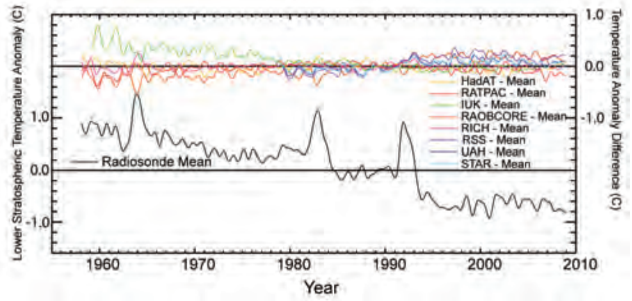

Fig. 2.6. As Fig. 2.4. but all time series are for the layer sampled by MSU channel 4, spanning 10–25 km in altitude, with a peak near 18 km. Additional dataset is STAR (Zou et al. 2008) and RSS Channel 4 is described in Mears and Wentz (2009b).

in the 1960s when the radiosonde network began to offer reasonably global monitoring. The cooling occurred in steps (Ramaswamy et al. 2006; Seidel and Lanzante 2004). Major volcanic eruptions (Agung 1963; El Chichon 1982; Pinatubo 1991) warmed the lower stratosphere for about two years (Free and Lanzante 2009), followed by cooler mean states than before (Fig. 2.6). Volcanic warming events are most notable in the tropics (Fig. 2.7). Other influences on stratospheric temperature changes include greenhouse gas and stratospheric ozone changes and solar variations.

This general evolution of global lower stratospheric temperature is robustly captured in all available radiosonde (1958–present) and satellite (1979–present) datasets (Fig. 2.6). However, the datasets differ in detail. Of those that cover 1979–2008, 2008 ranks as the coldest year in three, the second coldest in one, and the eighth coldest in another. Trends estimated from the average of the radiosonde datasets are −0.35 ± 0.07 °C decade^{-1} for 1958–2008, and −0.50 ± 0.16°C decade^{-1} for 1979–2008; however, there are statistically significant differences (of about 0.1°C decade^{-1}) between datasets, with all satellite-based datasets showing less cooling (−0.33° to 0.42°C decade^{-1}) since 1979 than the radiosondes, and even greater disagreement among the radiosonde datasets before that. This uncertainty in the magnitude, and therefore cause, of the long-term trend (Thorne et al. 2005a) is due to the lack of reference quality observations. However, 2008 saw the implementation of a new GCOS Reference Upper-Air Network to provide much higher-quality data, in both the troposphere and stratosphere (Seidel et al. 2009).

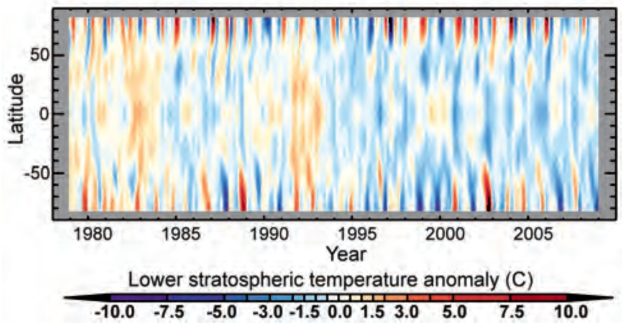

Fig. 2.7. As Fig. 2.5 but for the lower stratospheric channel (Mears and Wentz 2009b).

The tropical stratospheric QBO in wind direction (Baldwin et al. 2001) imposes a signature on tropical temperatures (Fig. 2.7), also apparent in the global average (Fig. 2.6). The QBO shifted from easterly to westerly in the lower stratosphere during 2008, bringing a change from cold to warm tropical anomalies. Sudden stratospheric warming events in northern high latitudes in January and February brought temperature increases of 10° to 30°K at the 10-hPa level (NOAA CPC 2009a). Their impact is seen in the annual anomaly map for the lower stratosphere (Plate 2.1, panel 1) as warm anomalies over the Canadian Arctic. Over Antarctica, the wintertime stratospheric vortex was the longest-lived since 1979, contributing to 2008 being one of the coldest winters on record in the Antarctic stratosphere and to a long-lived Antarctic ozone hole (NOAA CPC 2009b).

The preceding analysis focused on the lower stratosphere. The state of the global stratosphere at higher levels is more difficult to describe because few long-term datasets are available. The recent comprehensive analysis by the Stratospheric Processes and their Role in Climate program (Randel et al. 2009) included revised and updated data for the middle and upper stratosphere from the satellite-borne SSU for 1979–2005 (Shine et al. 2008). SSU data require homogeneity adjustments for instrument change and drift and for changing atmospheric composition, but they have not yet benefitted from analysis by multiple groups, which tends to facilitate the identification and correction of errors. The revised SSU data indicate long-term cooling of ~0.5° to 1.5°K decade^{-1} of the middle and upper stratosphere (about twice as large as lower stratospheric trends), but relatively constant temperatures during 1995–2005 like both MSU and radiosonde data for the lower stratosphere. However, the SSU channel that samples the lower stratosphere indicates a gradual temperature increase during that period, so there remain unreconciled differences with other datasets and uncertainty in middle and upper stratospheric temperature changes.

DO GLOBAL TEMPERATURE TRENDS OVER THE LAST DECADE FALSIFY CLIMATE PREDICTIONS?—J. KNIGHT, J. J. KENNEDY, C. FOLLAND, G. HARRIS, G. S. JONES, M. PALMER, D. PARKER, A. SCAIFE, AND P. STOTT

Observations indicate that global temperature rise has slowed in the last decade (Fig. 2.8a). The least squares trend for January 1999 to December 2008 calculated from the HadCRUT3 dataset (Brohan et al. 2006) is +0.07±0.07°C decade^{-1}—much less than the 0.18°C decade^{-1} recorded between 1979 and

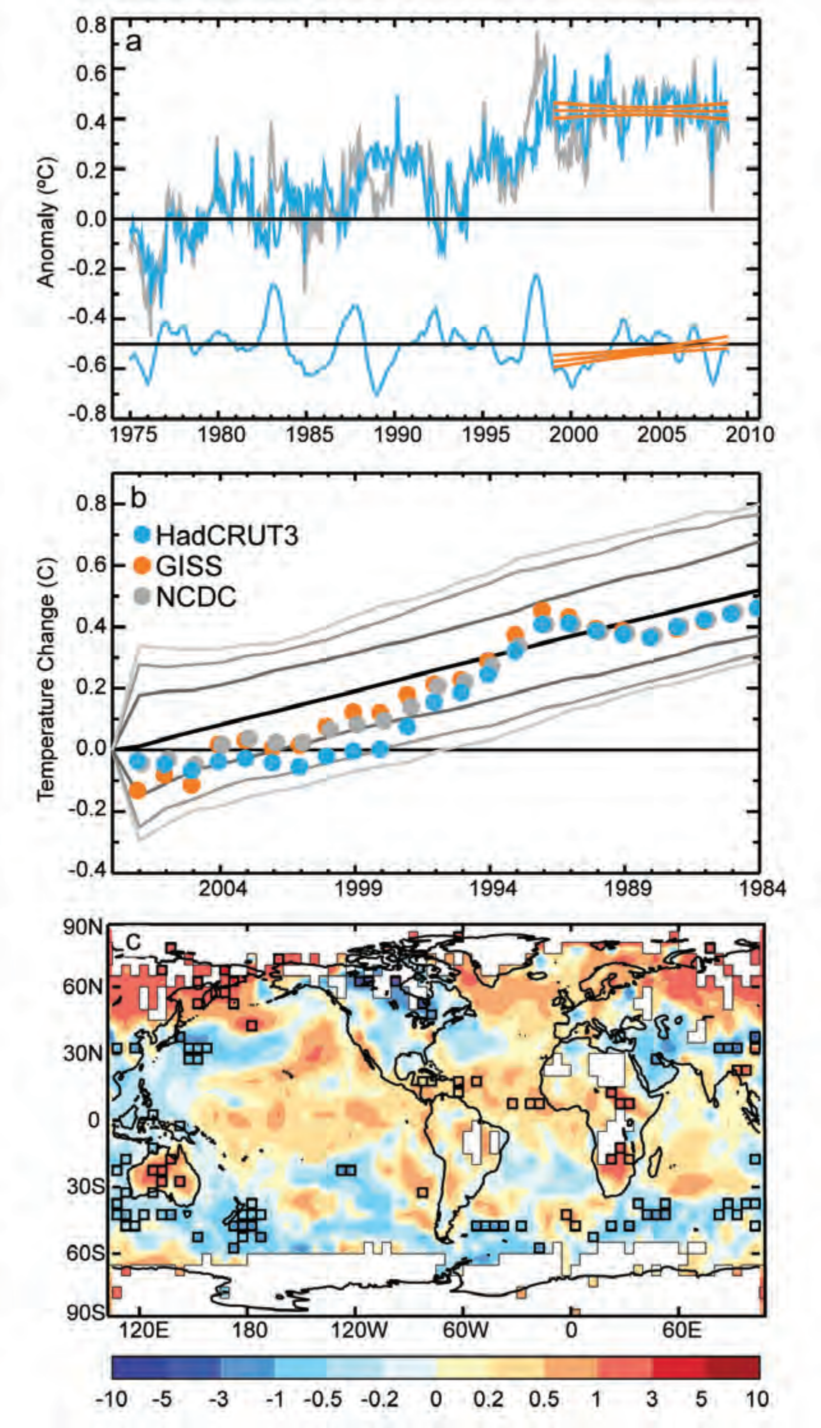

Fig. 2.8. Global mean temperature changes over the last decade in context. (a) Monthly global mean temperature anomalies (with respect to 1961–90 climatology) since 1975, derived from the combined land and ocean temperature dataset HadCRUT3 (gray curve). (top blue curve) The global mean after the effect of ENSO that has been subtracted is also shown, along with (bottom blue curve, offset by 0.5°C) the ENSO contribution itself. Least squares linear trends in the ENSO and ENSO-removed components for 1999–2008 and their two std dev uncertainties are shown in orange. (b) ENSO-adjusted global mean temperature changes to 2008 as a function of starting year for HadCRUT3, GISS dataset (Hansen et al. 2001) and the NCDC dataset (Smith et al. 2008) (dots). Mean changes over all similar-length periods in the twenty-first century climate model simulations are shown in black, bracketed by the 70%, 90%, and 95% intervals of the range of trends (gray curves). (c) Distribution of 1999–2008 trends in HadCRUT3 (°C decade^{-1}). Black squares indicate where the trends are inconsistent at the two std dev level with trends in 17 simulated decades (see text).

2005 and the 0.2°C decade^{-1} expected in the next decade (IPCC; Solomon et al. 2007). This is despite a steady increase in radiative forcing as a result of human activities and has led some to question climate predictions of substantial twenty-first century warming (Lawson 2008; Carter 2008).

El Niño–Southern Oscillation is a strong driver of interannual global mean temperature variations. ENSO and non-ENSO contributions can be separated by the method of Thompson et al. (2008) (Fig. 2.8a). The trend in the ENSO-related component for 1999–2008 is +0.08±0.07°C decade^{-1}, fully accounting for the overall observed trend. The trend after removing ENSO (the "ENSO-adjusted" trend) is 0.00°±0.05°C decade^{-1}, implying much greater disagreement with anticipated global temperature rise.

We can place this apparent lack of warming in the context of natural climate fluctuations other than ENSO using twenty-first century simulations with the HadCM3 climate model (Gordon et al. 2000), which is typical of those used in the recent IPCC report (AR4; Solomon et al. 2007). Ensembles with different modifications to the physical parameters of the model (within known uncertainties) (Collins et al. 2006) are performed for several of the IPCC SRES emissions scenarios (Solomon et al. 2007). Ten of these simulations have a steady long-term rate of warming between 0.15° and 0.25°C decade^{-1}, close to the expected rate of 0.2°C decade^{-1}. ENSO-adjusted warming in the three surface temperature datasets over the last 2–25 yr continually lies within the 90% range of all similar-length ENSO-adjusted temperature changes in these simulations (Fig. 2.8b). Near-zero and even negative trends are common for intervals of a decade or less in the simulations, due to the model's internal climate variability. The simulations rule out (at the 95% level) zero trends for intervals of 15 yr or more, suggesting that an observed absence of warming of this duration is needed to create a discrepancy with the expected present-day warming rate.

The 10 model simulations (a total of 700 years of simulation) possess 17 nonoverlapping decades with trends in ENSO-adjusted global mean temperature within the uncertainty range of the observed 1999–2008 trend (−0.05° to 0.05°C decade^{-1}). Over most of the globe, local surface temperature trends for 1999–2008 are statistically consistent with those in the 17 simulated decades (Fig. 2.8c). Field significance (Livezey and Chen 1983) is assessed by comparing the total area of inconsistent grid boxes with the range of similar area values derived by testing the consistency of trends in each simulated decade with those in the remaining simulated decades. The 5.5% of the data area that is inconsistent in the observed case is close to the median of this range of area values, indicating the differences are not field significant. Inconsistent trends in the midlatitude Southern Hemisphere strongly resemble the surface temperature pattern of the negative phase of the SAM (Ciasto and Thompson 2008), which did indeed show a negative trend in the last decade.

These results show that climate models possess internal mechanisms of variability capable of reproducing the current slowdown in global temperature rise. Other factors, such as data biases and the effect of the solar cycle (Haigh 2003), may also have contributed, although these results show that it is not essential to invoke these explanations. The simulations also produce an average increase of 2.0°C in twenty-first century global temperature, demonstrating that recent observational trends are not sufficient to discount predictions of substantial climate change and its significant and widespread impacts. Given the likelihood that internal variability contributed to the slowing of global temperature rise in the last decade, we expect that warming will resume in the next few years, consistent with predictions from near-term climate forecasts (Smith et al. 2007; Haines et al. 2009). Improvements in such forecasts will give greater forewarning of future instances of temporary slowing and acceleration of global temperature rise, as predicted to occur in IPCC AR4 projections (Easterling and Wehner 2009).

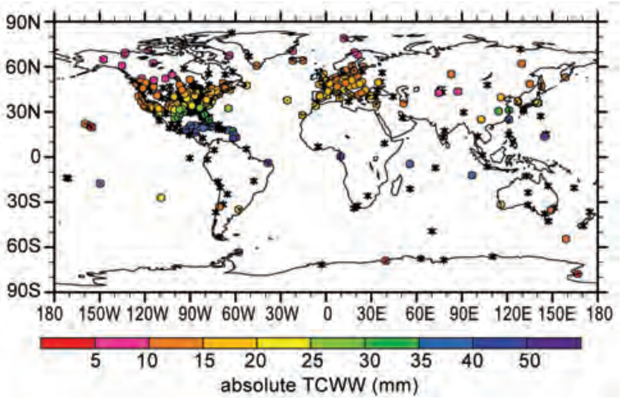

Fig. 2.9. 2008 annual mean TCWV (mm) at 252 stations (colored circles) and 308 stations (denoted by an asterisk) that have data in 2008, but not enough to calculate an annual mean.

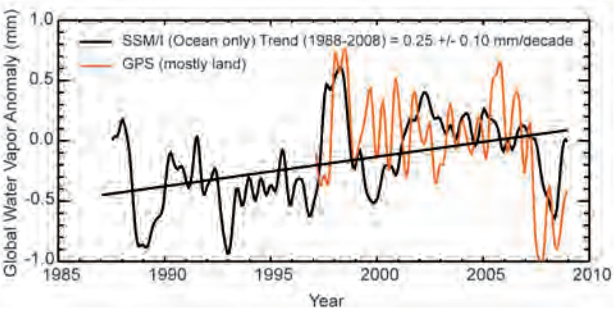

Fig. 2.10. Anomaly time series of TCWV both from SSM/I and from an average of GPS stations. The time series have been smoothed to remove variability on time scales shorter than 6 months. A linear fit to the SSM/I data is also shown, indicating an increasing trend in water vapor over the 1988–2008 period.

c. *Hydrological cycle*

1) Total column water vapor—C. Mears, J. Wang, and L. Zhang

Total column water vapor over the world's oceans has been monitored continuously since the launch of the first SSM/I satellite in late 1987 (Wentz 1997). These data have been independently evaluated and found to be accurate enough for climate studies (Trenberth et al. 2005). Beginning in the late 1990s, ground-based GPS measurements have provided a second accurate estimate of TCWV over land (Wang et al. 2007); they are an important complement to the ocean-only SSM/I measurements.

Plate 2.1, panel 5 includes data from SSM/I and from a subset of 71 GPS stations with continuous data from 1997 to 2008, allowing meaningful anomaly estimates. The network is expanding rapidly. In 2008 a total of 560 GPS stations had data, and annual means could be calculated at 252 stations (Fig. 2.9). There is generally agreement within 0.5 mm between the SSM/I and GPS measurements where they overlap. The most striking feature is the large dry anomaly centered on the central tropical Pacific, associated with La Niña. The dry region extends poleward and eastward from this source, resulting in dry anomalies over much of the continental United States.

The global ocean average SSM/I TCWV shows dramatic maxima in 1988–89 and 1997–98 associated with ENSO events (Fig. 2.10). Minima associated with La Niña events occur in 1988–89, 1993, 1999, and 2008. The GPS data averaged over the 71 stations in Plate 2.1 show similar features despite the substantially different geographical sampling. The SSM/I data show a 0.25 mm decade^{-1} trend in TCWV. In the tropics this is consistent with increases in lower tropospheric temperature (Mears et al. 2007) and has been formally attributed to anthropogenic change over the 1988–2006 period (Santer et al. 2007). Variability in zonally averaged TCWV is dominated by variability in the tropics caused by ENSO events (Fig. 2.11). The tropics dominate because of the larger changes in TCWV per degree change in temperature at higher temperatures as described by the Clausius–Clapeyron relationship.

2) Global precipitation—D. H. Levinson, K. A. Hilburn, and M. C. Kruk

Land-based data are primarily analyzed from monthly totals of in situ gauge measurements using the GHCN dataset (Peterson and Vose 1997), which for most regions extends back to the beginning of the twentieth century. Several alternative land-based datasets are also considered. Over ocean basins, three satellite datasets are considered:

- Remote Sensing Systems intercalibrated passive microwave rain retrievals (Hilburn and Wentz

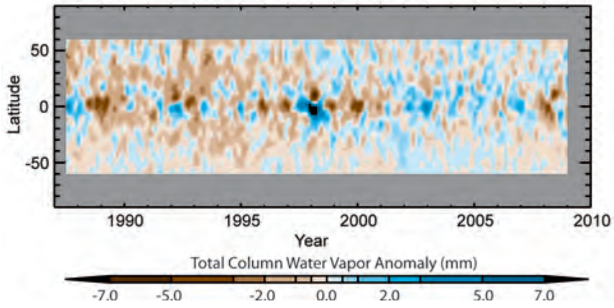

Fig. 2.11. Time–latitude plot of TCWV anomaly calculated using a reference period of 1988–2007. The data have been smoothed in the time direction to remove variability on time scales shorter than 4 months.

2008) that closely match gauges on tropical buoys (Bowman et al. 2009) and are not sensitive to snow, which may account for an apparent low global bias (Wentz et al. 2007)

- The Global Precipitation Climatology Project Version 2, Combined Precipitation Data Set (Adler et al. 2003), a combination of data from microwave and infrared satellite sensors and rain gauges
- NOAA CMAP (Xie and Arkin 1997), combining data from microwave and infrared satellite sensors, rain gauges, and numerical model predictions.

Despite obvious differences among datasets, global land precipitation has clearly varied on interdecadal time scales, and the above-average anomaly in 2008 is part of a longer-term wet period that began in the late 1990s (Fig. 2.12). The 2008 anomaly was dominated by an extremely wet Southern Hemisphere summer (DJF). There is substantial disagreement among the ocean precipitation time series, especially in the first half of the period (Fig. 2.12c). Despite this, RSS and GPCP have similar overall linear trends, both of which are significant at the 95% confidence level. The trend for CMAP is negative but not significant. Significance is estimated from deviations from the linear fit, accounting for autocorrelation (Santer et al. 2000). For RSS, the 95% confidence interval is about 60% larger than that estimated by Wentz et al. (2007), who estimated the uncertainty in RSS by using deviations from hydrological balance.

Spatial trends in GHCN annual precipitation were determined for 1901–2008 and for 1989–2008 (Fig. 2.13). On the century time scale, most of the globe has trended toward wetter conditions, but with notable exceptions, including parts of southern Europe, most of Africa, southwestern Australia, and the west coast of South America. Drying trends were most prominent in the African Sahel, where drought dominated from the 1970s through the 1990s. Since 1989, however, the Sahel has trended wetter (Fig. 2.13b). Two regions that have become significantly drier over

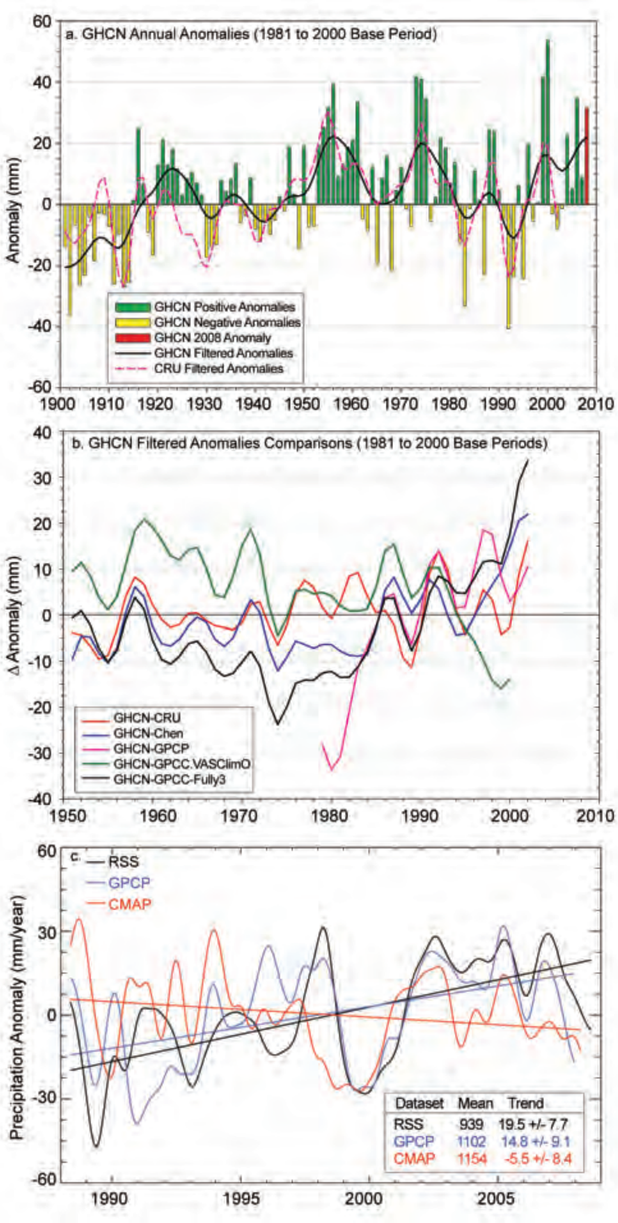

Fig. 2.12. (a) Annual global land surface precipitation anomalies (mm) over the period 1901–2008 from the GHCN dataset (Vose et al. 1992). Precipitation anomalies were calculated with respect to 1981–2000 (Trenberth et al. 2007): green bars are positive anomalies, yellow bars are negative anomalies, and red bar is 2008 anomaly. Smoothed GHCN and CRU (v.3) annual values were created using a 13-point binomial filter. (b) Time series of the difference between the smoothed GHCN annual anomalies and annual anomalies over global land areas from five different global precipitation datasets for the period 1951–2008: CRU v.3, Chen et al. (2002), GPCP, and two from the GPCC (VasClimO and Full v.3). (c) Ocean precipitation anomalies relative to the period 1988–2008. Averages are for the global ocean between 60°S and 60°N latitude using a common definition of "ocean." The annual cycle has been removed and the time series have been low-pass filtered by convolution using a Gaussian distribution, with 4-month width at half-peak power. Note that the RSS data are available through all of 2008, while GPCP and CMAP data are available through Apr and Jul 2008, respectively. The inset gives the 1988–2008 mean (mm yr^{-1}) and the linear trend (mm yr^{-1} $decade^{-1}$) with the 95% confidence interval. Straight lines denote the linear trends, and the confidence interval is estimated based on deviations from the linear fit and does not incorporate a particular dataset's "error."

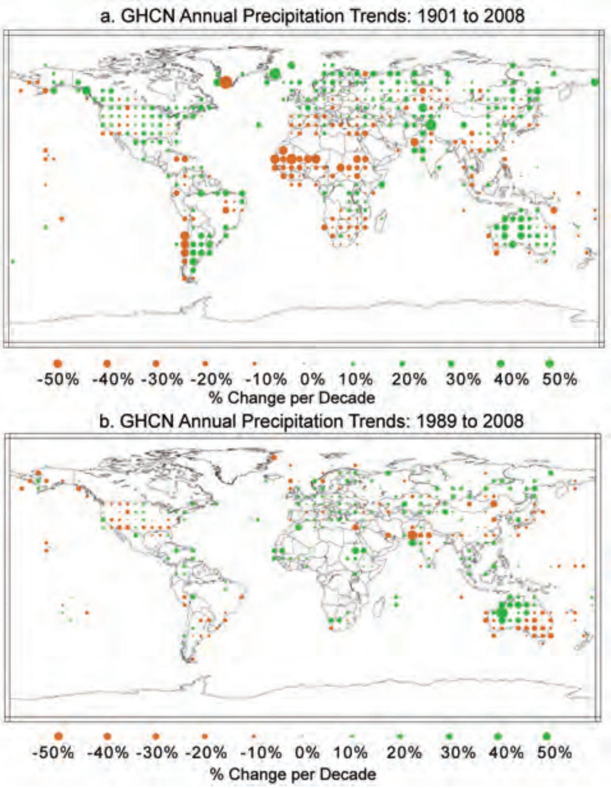

Fig. 2.13. Trends in annual precipitation calculated from the GHCN monthly dataset for two different time periods: (a) 1901–2008 (% change century^{-1}) and (b) 1989–2008 (% change decade^{-1}). Calculation of grid cell trends required at least two-thirds (66%) of the years without missing data during each of the two periods analyzed.

Fig. 2.14. (a) Time–latitude plot of GHCN annual land precipitation in terms of the % departure from 1989 to 2000 base-period means, with zonal means determined over 5°-latitude bands covering the period 1901–2008. Gray shading at higher latitudes in the early twentieth century is due to a lack of data south of 40°S and north of 75°N. (b) Same as (a) but for the RSS satellite record era. (c–e) Time–latitude section of precipitation anomalies (mm yr^{-1}) averaged over the (c) Atlantic, (d) Pacific, and (e) Indian Ocean basins as observed by the RSS monthly averaged dataset. Anomalies were calculated using the 1988–2008 base period by removing the latitude-dependent annual cycle.

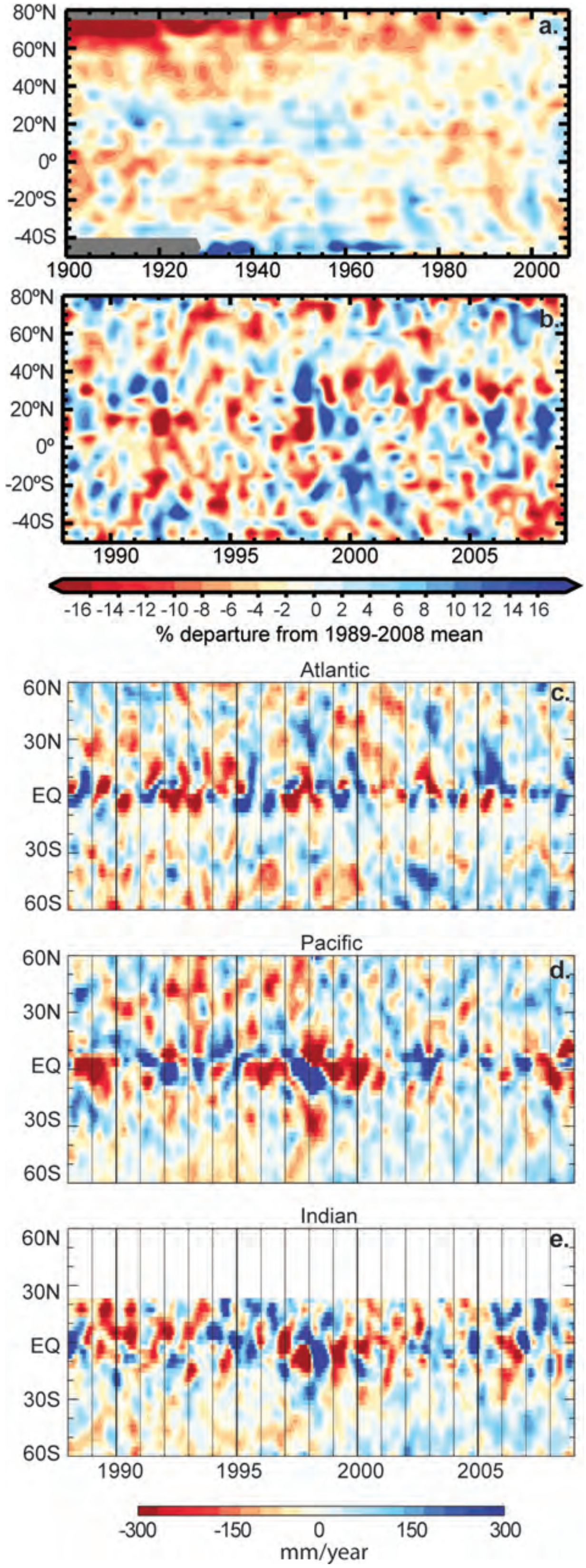

the past two decades are the southwestern United States and southeastern Australia.

These regional trends are also apparent in the GHCN zonal mean precipitation (Figs. 2.14a,b). A trend toward drier tropical conditions since the 1950s is clearly evident. There has been a steady increase in precipitation over northern high latitudes during the twentieth century, which has accelerated over the past 5 yr. Figures 2.14c–e show time–latitude sections of precipitation anomalies over the Atlantic, Pacific,

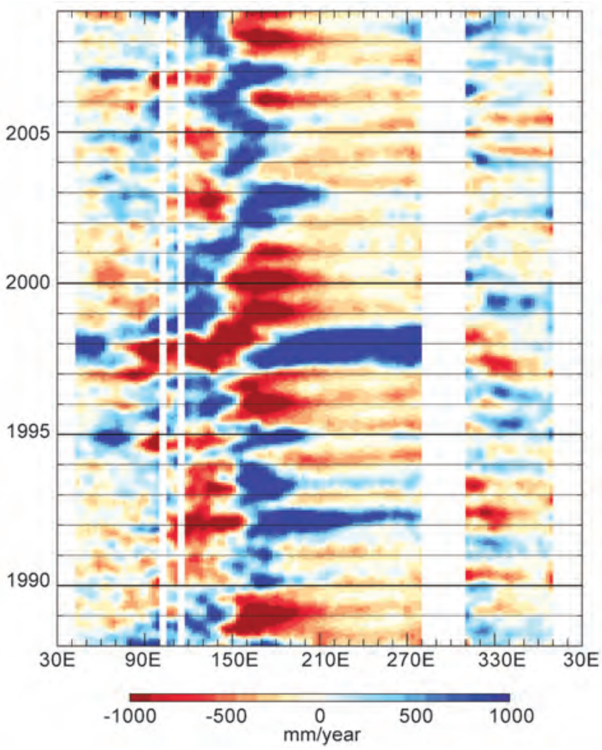

Fig. 2.15. Time–longitude section of precipitation anomaly averaged over the tropical ocean (5°S to 5°N) as observed by the RSS monthly averaged dataset. Anomalies were determined using the 1988–2008 base period by removing the longitude-dependent annual cycle. Missing areas are the results of land masks: between 10° and 40°E are due to Africa, the areas near 100° and 115°E are due to Sumatra and Borneo, and the areas between 280° and 310°E are due to South America.

and Indian Ocean basins over the shorter satellite era. Wetter-than-average conditions over the Atlantic basin in 2008 were focused south of the equator in the first half of 2008, and north of the equator for the second half. With the break in the dry conditions over the equatorial Pacific in the middle of 2008, the drier areas shifted northward.

The western equatorial Pacific was wetter than normal in 2008, while it was drier than normal across much of the tropical eastern and central Pacific (Plate 2.1, panel 6), an expected consequence of the 2008 La Niña (Ropelewski and Halpert 1987). The dry anomalies across the central Pacific began in late 2007 (Fig. 2.15) and strengthened in the beginning of 2008 before weakening around June. Dry conditions redeveloped later in 2008 but were not as strong.

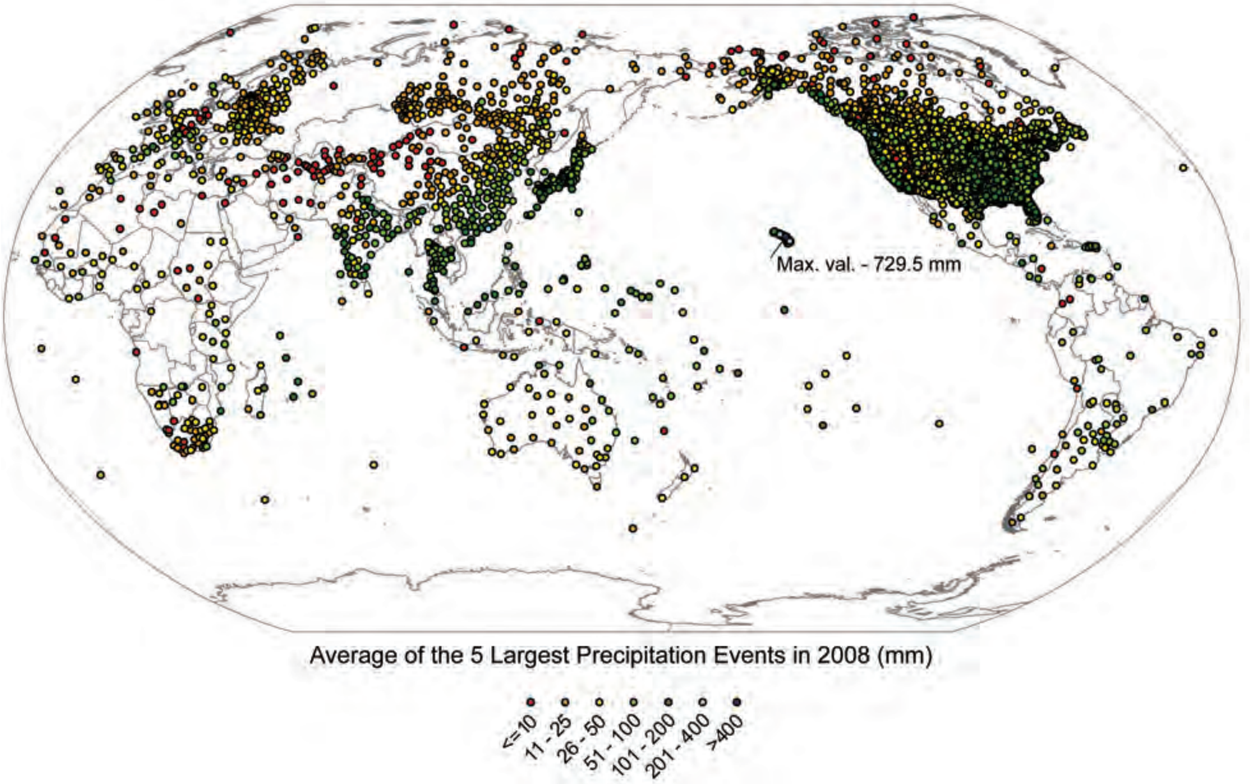

Fig. 2.16. Global map of daily precipitation extremes observed in 2008 from the GHCN dataset. The plotted values are the average of the top five largest daily precipitation events (mm) at each station.

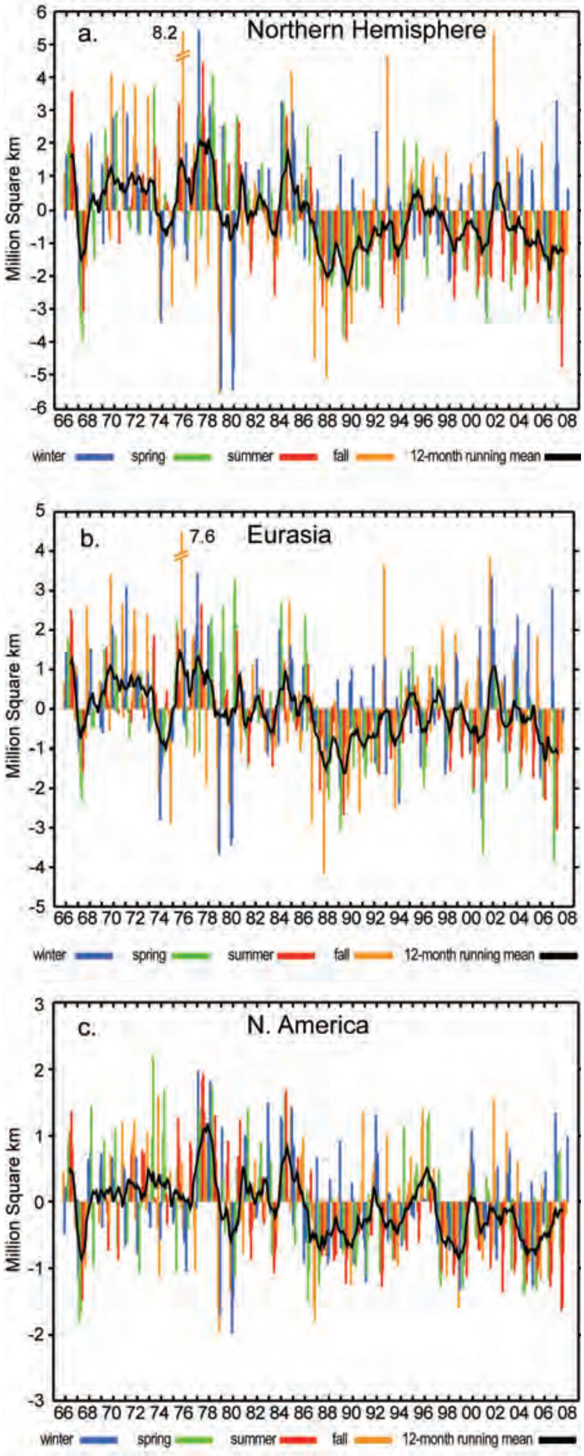

Fig. 2.17. Anomalies of monthly snow cover extent over Northern Hemisphere lands (including Greenland) between Nov 1966 and Dec 2008. Anomalies are calculated from NOAA snow maps. Mean hemispheric snow extent is 25.5 million km^2 for the full period of record. Monthly means for the period of record are used for nine missing months between 1968 and 1971 to create a continuous series of running means. Missing months fall between Jun and Oct; no winter months are missing.

The most extreme land precipitation events observed in 2008 were determined by averaging the five wettest days using GHCN data. The largest extremes affected Japan, Southeast Asia, and numerous locations across the United States (Fig. 2.16). The maximum of 716 mm occurred in the Hawaiian Islands.

3) Northern Hemisphere continental snow cover extent—D. A. Robinson

Annual snow cover extent over the Northern Hemisphere was 1.1 million km^2 less than the 39-yr average; 2008 had the fourth least extensive cover on record (Table 2.1). This includes the Greenland ice sheet. The 12-month running means of SCE were below the long-term average throughout 2008. They were consistently the lowest values since the notable minimum in the late 1980s and early 1990s (Fig. 2.17).

The year commenced with record maximum hemispheric SCE, due to record Eurasian cover (Fig. 2.17b; see also box in regional chapter on the impacts). February SCE remained anomalously large over both continents. Combined with an upper-quartile ranking in December 2007, the winter of 2007/08 had the fourth most extensive hemispheric SCE of the past 42 years (Fig. 2.18). Eurasian snow melted quickly in March, leading to a record low SCE over the continent and the fourth lowest over the hemisphere. In May, North American SCE joined Eurasia and the hemisphere as a whole in the lowest quartile. Record-low June coverage occurred over both continents. Spring coverage was the third lowest on record, and summer SCE was a record low.

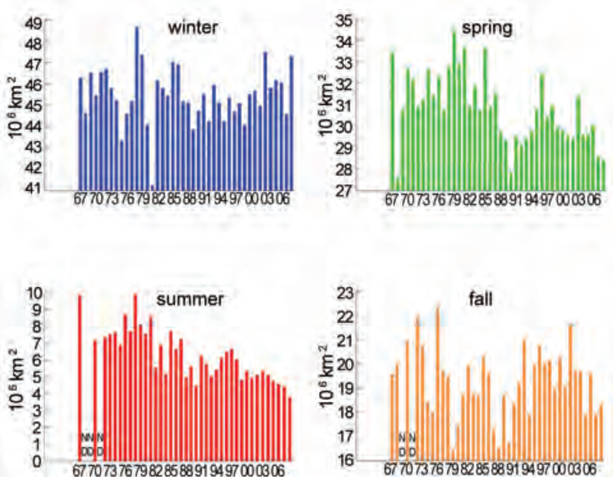

Fig. 2.18. Seasonal snow cover extent over Northern Hemisphere lands (including Greenland) between winter (Dec–Feb) 1966/67 and fall (Sep–Nov) 2008. Calculated from NOAA snow maps.

Table 2.1. Monthly and annual climatological information on Northern Hemisphere and continental snow extent between Nov 1966 and Dec 2008. Included are the numbers of years with data used in the calculations, means, std dev, 2008 values, and rankings. Areas are in millions of square kilometers. 1968, 1969, and 1971 have 1, 5, and 3 missing months, respectively, and thus are not included in the annual (Ann) calculations. North America (N. Am.) includes Greenland. Ranks are from most extensive (1) to least (ranges from 39 to 43 depending on the month).

	Years	Mean	Std dev	2008	2008 Northern Hemisphere rank	Eurasia rank	N. Am. rank
Jan	42	47.0	1.6	50.1	1	1	13
Feb	42	45.9	1.8	47.4	11	13	10
Mar	42	40.9	1.9	37.9	39	42	7
Apr	42	31.3	1.7	29.4	36	42	9
May	42	20.3	1.9	17.7	38	38	34
Jun	41	10.8	2.2	6.6	41	41	41
Jul	39	4.7	1.5	2.4	39	39	39
Aug	40	3.4	1.0	2.4	35	38	34
Sep	40	5.6	1.0	5.1	26	30	17
Oct	41	18.3	2.6	16.8	33	31	26
Nov	43	34.1	2.0	32.8	32	32	25
Dec	43	43.5	1.8	43.9	22	32	7
Ann	39	25.5	1.0	24.4	36	36	25

Eurasian cover consistently ranked near the 25th percentile throughout the fall and into December. North American SCE was slightly above average in September, somewhat below average in October and November, and seventh most extensive in December. This resulted in hemisphere-wide cover between the 20th and 50th percentile during the last four months of 2008, and a fall cover ranking as 10th lowest.

4) Global cloudiness—M. J. Foster, S. A. Ackerman, R. Bennartz, A. K. Heidinger, B. C. Maddux, and W. B. Rossow

Global cloudiness in 2008 was dominated by La Niña, a return of Arctic summer cloudiness due to a weakening of the anticyclonic atmospheric circulation pattern seen in 2007, and an increase in the amount of equatorial Atlantic high cloud in the boreal spring. The primary dataset used for this analysis is the 27-yr record of cloud retrievals in NOAA's AVHRR PATMOS-x dataset.

The La Niña, along with enhanced low-level easterly winds, strengthened large-scale convection in the western Pacific near Indonesia and suppressed it in the central Pacific. Plate 2.1, panel 4 shows below-normal cloudiness in the central equatorial Pacific, and above-normal cloudiness around Indonesia. The magnitude of the central Pacific negative anomaly is approximately 20%–25%. The positive anomaly around Indonesia is between 10% and 15%. Only small portions of the central Pacific negative anomaly are statistically significant at the 95% confidence level, and none of the positive anomaly around Indonesia is statistically significant.

Both MODIS and PATMOS-x capture a positive equatorial anomaly in boreal spring and summer 2008 (Fig. 2.19). This is consistent with an anomalous shift of the ITCZ over the equatorial Atlantic, which may have been influenced by ENSO effects on the Walker circulation (Saravanan and Chang 2000; Chiang et al. 2002). NCEP–NCAR reanalysis data show higher-than-normal SSTs, easterly wind strength, and tropospheric humidity, yielding increased convective activity and a positive high cloud anomaly over 30% relative to the long-term mean for March through May. The magnitude of the anomaly is reduced in Fig. 2.19 by an ENSO-induced negative high cloud anomaly in the equatorial central Pacific, but portions of the annual anomaly are statistically significant at the 95% confidence level.

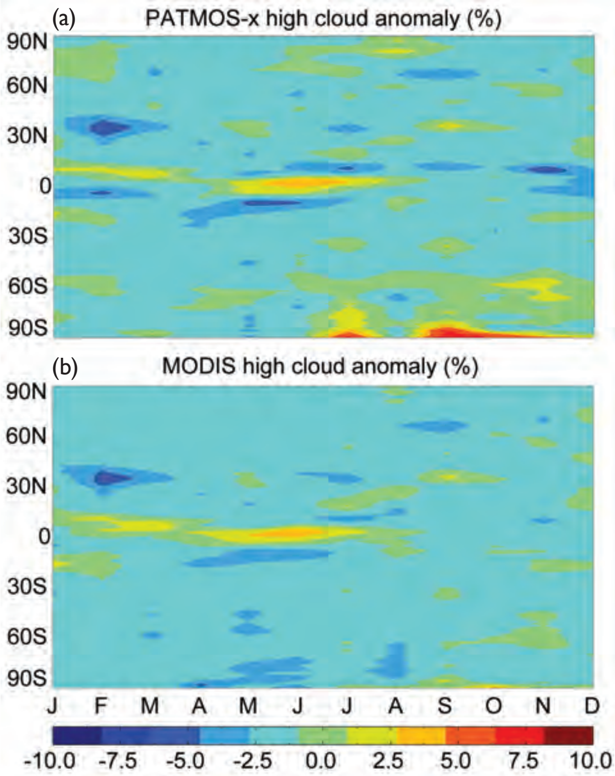

Fig. 2.19. (a) Monthly zonal average PATMOS-x anomalies of high cloud cover (cloud top pressure < 440 hPa) in 2008, relative to 2003–08 climatology based on retrievals from the NOAA-16 and NOAA-18 satellites. The 2003–08 reference period is chosen to match that of MODIS (b) to facilitate comparison. (b) Same as (a) but for MODIS (cloud top pressure < 440 hPa) based on retrievals from the *Aqua* and *Terra* satellites.

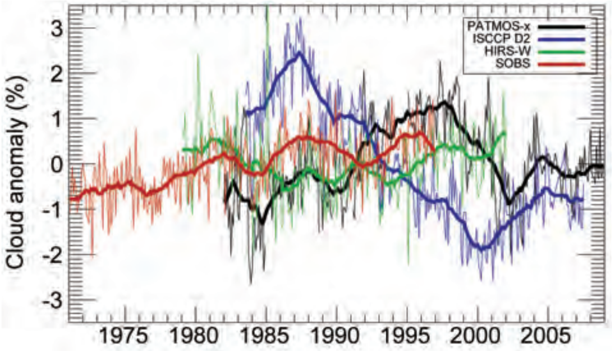

Fig. 2.20. Anomalies of monthly cloud amount between Jan 1971 and Dec 2008 taken from four datasets. The thick solid lines represent smoothing with a boxcar filter with a 2-yr window. There are 6 months missing from the PATMOS-x time series between Jan 1985 and Feb 1991, as well as a gap from Jan 1994 to Feb 1995.

In 2007 increased temperatures and decreased tropospheric humidity associated with an anticyclonic atmospheric circulation pattern caused noticeable decreases in Arctic summer cloudiness (Kay et al. 2008). In 2008 this anticyclonic atmospheric circulation pattern persisted through boreal spring but weakened during the Arctic summer, resulting in an increase in cloudiness over northern Greenland and much of the Arctic Ocean of 15% to 20%. None of these increases is statistically significant.

Figure 2.20 shows global mean monthly cloud amount anomalies since January 1971 from four sources: SOBS for 1971–96, infrared sounder instruments on the NOAA polar orbiting weather satellites (HIRS-W) for 1979–2002, imaging radiometers on operational weather satellites (ISCCP) for 1983–2007 (and continuing), and the PATMOS-x data. The records appear to disagree on the long-term variation of cloudiness, but the variations and their differences are smaller than the estimated uncertainties and are much smaller than the annual cycle. We conclude that the global monthly mean cloud cover did not vary by more than a few percent over more than two decades. This upper limit is significant in light of other, simultaneous variations of the climate: the lack of change needs to be explained as much as would a significant change.

PATMOS-x is the only record shown that currently extends throughout 2008. Its 2008 annual mean globally averaged cloud amount is 65%, very close to its 27-yr mean of 65.2; all months were within 1% of the long-term mean cloudiness.

5) River discharge—A. M. Macdonald, B. M. Fekete, L. C. Bowling, R. B. Lammers, R. Lawford

Discharge is a uniquely useful climate indicator among water cycle components as hydrograph observations integrate both in space and time. Runoff varies in response to natural and anthropogenic forcing (e.g., land-use change, reservoirs, dams) (Milliman et al. 2008; IPCC 2007; Gedney et al. 2006). Variations that affect the water available in local watersheds contribute to changes in ocean freshwater budgets (Talley 2008; Peterson et al. 2006), and play a significant role in the temporal variability and trends of the global water cycle (Oki and Kanae 2006). Modern estimates of global runoff vary by less than 10% (Table 2.2). Regional year-to-year discharge is dominated by variations in precipitation but is also nonlinearly dependent on groundwater contributions, regional runoff fractions, and surface water withdrawals.

Most discharge records have temporal gaps and/or infrequent or spatially inhomogeneous sampling. Divergent methods of data collection and apparent political disincentives to report accurately com-

TABLE 2.2. Estimates of long-term mean annual global runoff ($km^3\ yr^{-1}$) into major ocean basins. Percent variation is a measure of the variation among the different estimates and is equal to the std dev divided by the mean times 100. Rows 1–3, 5, and 7 are adapted from Dai and Trenberth's (2002) Table 4, which states that the values exclude the Antarctic runoff into the Southern Ocean that they estimate at ~2614 $km^3\ yr^{-1}$ after Jacobs et al. (1992) (see their references). Rows 4, 6, and 8 are estimated from GRDC (2004). Including only those estimates made in the last decade reduces the percent variation among the estimates to 16%, 6%, 8%, 42%, 10%, and 4% for columns 1 to 6, respectively

	Arctic	*Atlantic*	*Indian*	*Mediterranean & Black Seas*	*Pacific*	*Total*
Baumgartner and Reichel (1975)	2,600	19,300	5,600	0	12,000	37,713
Korzun et al. (1977)	5,220	20,760	6,150	0	14,800	46,930
Oki (1999)	4,500	21,500	4,000	0	10,000	40,000
Shiklomanov (1999)	4,281	19,799	4,858	0	12,211	41,149
Fekete et al. (2000)	2,947	18,357	4,802	1,169	11,127	38,402
Fekete et al. (2002)	3,268	18,506	4,858	475	10,476	37,583
Dai and Trenberth (2002)	3,658	19,168	4,532	838	9,092	37,288 ±662
GRDC (2004)	3,863	20,373	5,051	0	11,245	40,533
Average, Std Dev and % Variation of above Values	3,792 ±863 23%	19,720 ±1,102 6%	4,981 ±653 13%	827 ±347 42%	11,369 ±1724 15%	39,950 ±3176 8%

pound the issue. Although satellite measurements may improve global coverage, orbit tracks present issues for spatial and temporal resolution (Alsdorf et al. 2007).

The primary archive for global in-situ river discharge data is the GRDC. As of December 2007, it held 3.3 million monthly discharge estimates from 7,332 stations in 156 countries worldwide, representing some 276,000 station years of data. The shortest records are for a single year, the longest 197 years. However, the most recent data available (GRDC 2009) are for 2004.

Planned discharge data products will combine discharge observations with rainfall runoff simulation based on meteorological observations to provide spatially distributed estimates (Fekete et al. 2001). Alsdorf and Lettenmeier (2003) also recommend incorporation of satellite estimates. As a precursor to such merged products, the Global Terrestrial Network for Hydrology publishes runoff and river discharge estimates based on climate and precipitation data forcing. There is strong spatial variability of 2007 runoff and anomalies (Fig. 2.21), reflecting the integral quality of discharge. Such products offer the potential for global monitoring, even where primary data are not readily accessible.

d. Atmospheric circulation

1) MEAN SEA LEVEL PRESSURE—R. Allan

The major feature of the 2008 annual global MSLP field was the influence of the moderate La Niña event. Annual MSLP anomalies were 1 to 2.5 hPa above average across the bulk of the Pacific Ocean and up to 1 hPa below average across the Indian Ocean and the "maritime continent" of Indonesia (Plate 2.1, panel 7). El Niño and La Niña events can be monitored by the SOI, the normalized MSLP difference between Tahiti and Darwin (Allan et al. 1996). El Niños (negative SOI) and La Niñas (positive SOI) vary in magnitude, duration, and evolution, and no two events or episodes are exactly the same. Major events can be near global in their influence on weather patterns, due

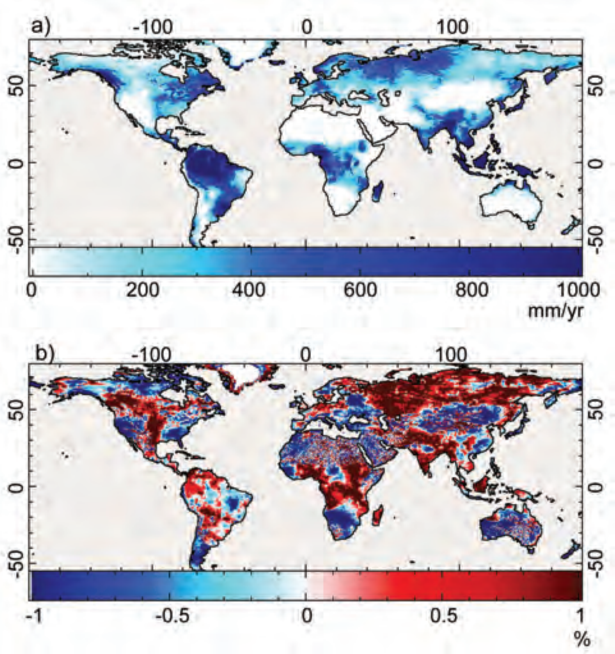

Fig. 2.21. Estimates for 2007 of (a) runoff and (b) its anomaly based on outputs from a hydrometeorological model utilizing GPCP precipitation measurements.

to dynamical teleconnections from the Indo-Pacific region to higher latitudes in both hemispheres. There are also protracted El Niño and La Niña episodes, such as the protracted El Niño in the first half of the 1990s and the protracted La Niña from 1998 to 2000 (Allan and D'Arrigo 1999; D'Arrigo et al. 2008). Such episodes are characterized by periods with weak–moderate anomalies, but their persistence over several years has substantial impacts. They also tend to show within-episode fluctuations, with measures such as the SOI suggesting that an episode can show signs of waning but then be reestablished. The SOI since 1900 is dominated by interannual to multidecadal vacillations, but very-long-term trends are not evident (Fig. 2.22). Figure 2.22b indicates that the weak–moderate La Niña in 2008 is part of a longer, persistent episode that started in 2007.

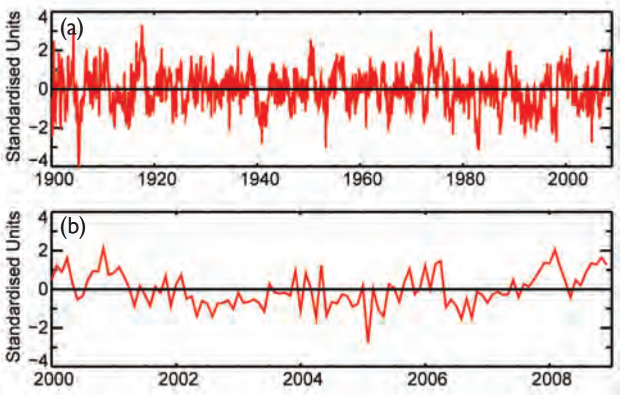

Fig. 2.22. The SOI for (a) 1900 to present and (b) from 2000 to 2008 relative to the 1876 to 2008 base period.

In the Southern Hemisphere in 2008, high latitudes were dominated by negative MSLP anomalies, with positive MSLP anomalies at middle latitudes, particularly across the southern Atlantic and Indian Ocean sectors (Plate 2.1, panel 7). This indicates a strong positive phase of the Southern annular mode (Fig. 2.23b) which plays an important role in modulating climatic patterns across the Southern Hemisphere continents. The 2008 annual MSLP anomalies in the North Atlantic region, being negative at higher latitudes and positive at midlatitudes, reflect a positive winter NAO (Fig. 2.23a). The instrumental NAO record is dominated by interannual to multidecadal fluctuations. The negative MSLP anomalies over the United Kingdom and Scandinavia in 2008 also reflect the circulation pattern underlying the wet 2008 summer in the United Kingdom.

2) Surface wind speed—C. Mears

Surface wind speed over the oceans began to be monitored continuously with the first SSM/I satellite in late 1987. This uses measurements of upwelling microwave radiation to infer the surface roughness of the world's oceans, and thus surface wind speed (Wentz 1997). Here we use Version 6 of the SSM/I dataset produced by RSS. The average winds over the global ocean exhibited a maximum in 1988–89, followed by an increasing trend since 1990 (Fig. 2.24). The sharp peak in mid-2008 may be an artifact of missing data in the SSM/I dataset, because the sharp peak is not seen in wind speeds derived from the QuikSCAT microwave scatterometer (Lungu and Callahan 2006).

Zonal mean surface wind speed is dominated by short-term variability that makes it difficult to discern interannual and decadal scale changes (Fig. 2.25). The only obvious long-term trend occurs in the southern extratropics. Hence, a large portion of the global scale increase is due to changes in this region, related to the intensification of the Antarctic circumpolar circulation (Yang et al. 2007; Fig. 2.23b). The effects of ENSO are difficult to discern in part because averaging over all available longitudes de-emphasizes the east–west movement of circulation features during ENSO.

Plate 2.1, panel 8 reveals several notable anomalies in 2008. A large positive anomaly occurred in the central tropical Pacific, associated with the La Niña.

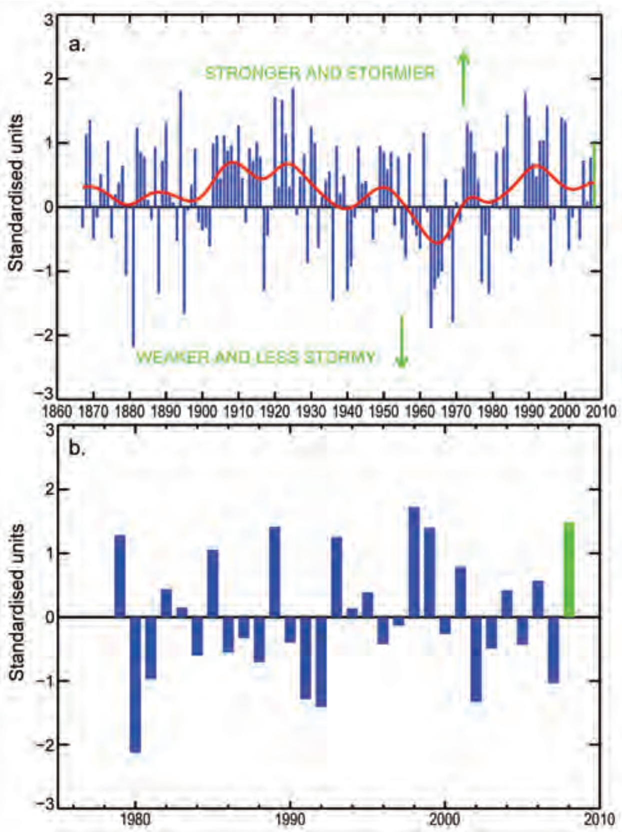

Fig. 2.23. (a) The annual historical instrumental [Ponta Delgada (Azores) minus Stykkisholmur (Iceland), normalized] NAO series from the mid-1860s to present (blue); the 21-point binomial filter run through the data three times (red). The green bar shows the average for the 2007/08 boreal winter. (b) Standardized 3-month running-mean value of the SAM or AAO index from 1979. The loading pattern of the SAM/AAO is defined as the leading mode of EOF analysis of monthly mean 700-hPa height during the 1979–2000 period. The monthly SAM/AAO index is constructed by projecting the monthly mean 700-hPa height anomalies onto the leading EOF mode. The resulting time series are normalized by the std dev of the monthly index (1979–2000 base period). Source: www.cpc.ncep.noaa.gov/products/precip/CWlink/daily_ao_index/aao/aao.shtml.

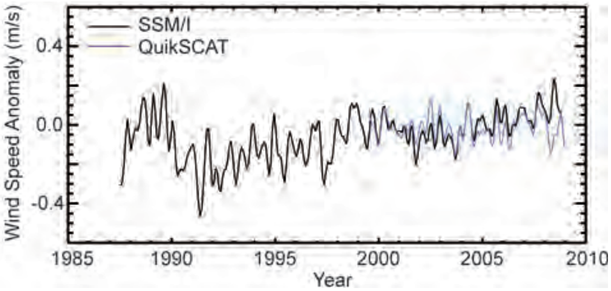

Fig. 2.24. Surface wind speed anomalies averaged over the global ice-free oceans. The time series has been smoothed to remove variability on time scales shorter than 4 months. The reference period for the SSM/I measurements is 1988–2007. For the QuikSCAT measurements the reference period is 2000–07, with the mean adjusted to match the SSM/I anomalies for the 2000–07 period.

A large negative anomaly affected most of the Northeastern Pacific, and there was a large positive anomaly over most of the Southern Ocean. In the North Atlantic, the positive anomalies near Iceland and in the trade wind region are consistent with the positive winter North Atlantic Oscillation (section 2d1; see also Hurrell et al. 2003).

e. *Earth radiation budget at top-of-atmosphere*—T. Wong, P. W. Stackhouse Jr., D. P. Kratz, and A. C. Wilber

Preliminary analysis suggests that global annual-mean outgoing longwave radiation decreased by ~0.75 W m^{-2}, from 2007 to 2008, while there was a decrease of 0.14 W m^{-2} in global-annual mean reflected shortwave radiation (Table 2.3). A small portion of the shortwave decrease was caused by changes in the total solar irradiance since the 11-yr solar cycle was near its minimum during 2007–08. The combined longwave and shortwave changes caused an increase of ~0.89 W m^{-2} in net radiation into the Earth climate system in 2008. However, these initial results are largely derived from the FLASHFlux dataset (Stackhouse et al. 2006; L'Ecuyer et al. 2009), which still includes instrument drift artifacts between September 2007 and December 2008 that are currently under study by the CERES instrument team and have not yet been removed. Reassessments of these results are expected when newer CERES data are released. Relative to the multidataset average for 2001 to 2008, the 2008 global annual-mean anomalies (Table 2.3) are −0.54/−0.26/+0.80 W m^{-2}

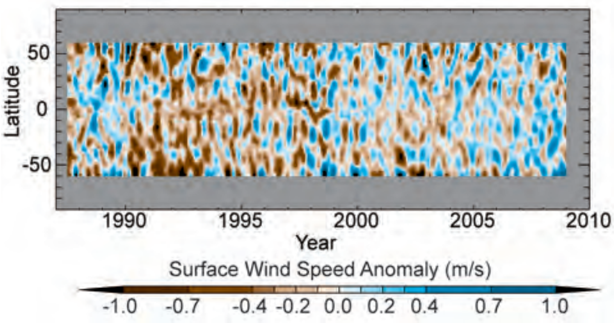

Fig. 2.25. Surface wind speed anomalies by latitude (reference period 1988–2007) over the ice-free oceans. The data have been smoothed in time to remove variability on time scales shorter than 4 months.

Table 2.3. Global annual-mean TOA radiative flux changes between 2007 and 2008, the 2008 global annual-mean radiative flux anomalies relative to their corresponding 2001–08 mean climatological values, and the 2σ interannual variabilities of 2001–08 global annual-mean fluxes (units in W m^{-2}).

	One year change (2008 minus 2007)	2008 anomaly (relative to climatology)	Interannual variability (2001 to 2008)
Longwave	−0.75	−0.54	±0.56
Shortwave	−0.14	−0.26	±0.41
Net	+0.89	+0.80	±0.82

respectively for longwave/shortwave/net radiation. These are within their corresponding 2σ interannual variabilities (Table 2.3) for this period.

Time series of global monthly mean deseasonalized anomalies since March 2000 have been constructed by merging ERB datasets from three sources: CERES EBAF (Loeb et al. 2009); CERES ERBE-like (Wielicki et al. 1999); and FLASHFlux (Fig. 2.26). The 2σ monthly uncertainties of the merge procedure is ±0.23/±0.93/±1.11 W m^{-2}, respectively, for the longwave/shortwave/net radiation. A decrease in longwave and increase in net radiation are noticeable in 2008 and are partly related to the switch to the 2007–08 La Niña, which altered the global distribution of clouds, total column water vapor, and temperature. Linear trend analyses are inconclusive due to natural fluctuation in ERB relating to ENSO activity, large uncertainty from the data-merging process, and instrument drift issues in the 2007–2008 FLASHFlux data. A long-term homogeneous data source with in-depth instrument stability analysis (e.g., CERES EBAF) is needed to reduce these uncertainties for future reassessment activity.

f. Atmospheric composition

1) Atmospheric chemical composition—R. C. Schnell

(i) Carbon dioxide, methane, and carbon monoxide—E. J. Dlugokencky

(a) Carbon dioxide

Since 1750, ~335 billion tons of carbon has been emitted into the atmosphere by combustion of fossil fuels and production of cement. About half of these emissions have occurred since the mid-1970s (Marland et al. 2008), and emission rates increased by >3% from 2000 to 2004 (Raupach et al. 2007). This carbon, which is emitted as CO_2, is partitioned into the atmosphere, oceans, and terrestrial biosphere. Atmospheric CO_2 has increased from about 280 ppm (ppm = parts per million by dry-air mole fraction) at the start of the Industrial Revolution to more than

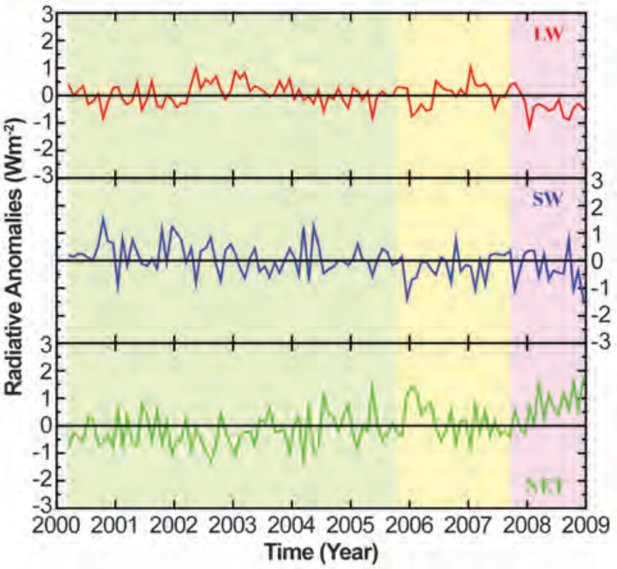

Fig. 2.26. Time series of global monthly mean deseasonalized anomalies of TOA Earth Radiation Budget for longwave (red line), shortwave (blue line), and net radiation (green line) from Mar 2000 to Dec 2008. Anomaly is computed relative to the calendar month climatology derived for the Mar 2000 to Dec 2008 period. The shaded green/yellow/pink area of the figure indicates the portion of the time series that is constructed using the CERES EBAF (Mar 2000 to Oct 2005)/CERES ERBE-like (Nov 2005 to Aug 2007)/FLASHFlux (Sep 2007 to Dec 2008) dataset, respectively. All three datasets are derived directly from CERES measurements. EBAF has been renormalized so that globally averaged top-of-atmosphere net radiation from 2000 to 2005 is consistent with ocean heat storage value (Willis et al. 2004; Hansen et al. 2005; Wong et al. 2006). The green (EBAF) and yellow (ERBE-like) shading indicate high-quality climate data with in-depth on-orbit instrument stability analysis. The pink shading (FLASHFlux) indicates preliminary climate data with possible instrument stability artifacts. Mean differences among datasets were removed using available overlapping data, and the combined ERBE time series was anchored to the absolute value of EBAF before deseasonalization.

380 ppm today. About half of the emitted CO_2 remains in the atmosphere after a year, and after a millennium, ~20% remains (Archer and Brovkin 2008). The atmospheric increase since the preindustrial era contributes ~1.7 W m^{-2} of radiative forcing (see, e.g., www.esrl.noaa.gov/gmd/aggi/).

The fate of fossil fuel–derived CO_2 is important to climate, because different reservoirs have different residence times and different susceptibilities to human interference. Therefore much current research is dedicated to understanding the partitioning of fossil CO_2 into the ocean and terrestrial biosphere. One key indicator of this is stable C isotopes in atmospheric CO_2. Figure 2.27 (top) shows CO_2 mole fraction and $\delta^{13}C$ in CO_2 from weekly samples at Cape Kumukahi, Hawaii. The long-term decline in $\delta^{13}C$ results from fossil carbon being depleted in ^{13}C relative to atmospheric CO_2. There is a seasonal cycle of opposite phase in CO_2 mole fraction and $\delta^{13}C$. As the biosphere takes up CO_2 in the spring and summer, it favors ^{12}C; this enriches the atmosphere in ^{13}C (less negative $\delta^{13}C$ values). Interannual variation in the balance between photosynthesis and respiration is seen in the subtle variations in the long-term $\delta^{13}C$ trends.

The preliminary globally averaged atmospheric CO_2 mole fraction in 2008 was 384.9 ppm, 2.28 ppm more than in 2007 (see www.esrl.noaa.gov/gmd/ccgg/trends/ for updated data; see Conway et al. 1994 for a description of sampling network and methods). This is significantly greater than the average rate of increase from 1979 through 2008, 1.62 ppm yr^{-1}. Despite fossil CO_2 emissions being predominantly in the Northern Hemisphere, the rate of increase of atmospheric CO_2 is approximately the same everywhere. Figure 2.28 shows monthly mean CO_2 mole fractions from four well-spaced NOAA ESRL observatories. The amplitude of the seasonal cycle varies according to exposure of air masses arriving at the sites to the terrestrial biosphere, but there are no significant differences in long-term trends.

(b) Methane (CH_4)

Methane contributes ~0.7 W m^{-2} to anthropogenic radiative forcing, when direct and indirect effects are included. While ~2/3 of CH_4 emissions are from anthropogenic sources, natural emissions of CH_4, predominantly from wetlands, are especially susceptible to climate change because they depend strongly on temperature and precipitation. In the Arctic, where surface temperatures are increasing at twice the global rate (Solomon et al. 2007), there is the potential for increases in CH_4 emissions from wetlands. The Arctic also contains large stores of organic carbon in permafrost (Zimov et al. 2006) and in hydrates (Kvenvolden 1993). Rapid destabilization of hydrates could release enormous amounts of CH_4 in a short time, although this scenario is unlikely. Anthropogenic sources such as biomass burning are also susceptible to changing climate through changes in precipitation. Dry conditions during the strong El Niño of 1997–98 resulted in an estimated 50% increase in CH_4 emissions from biomass burning in the tropics and high northern latitudes relative to normal (van der Werf et al. 2006).

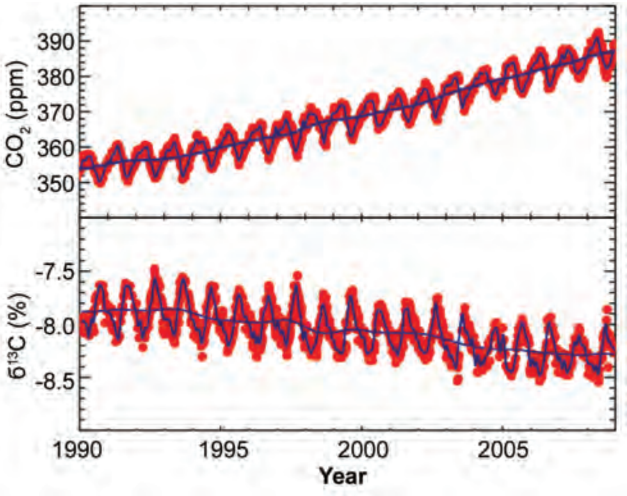

Fig. 2.27. CO_2 dry air mole fractions (top: NOAA ESRL) and $\delta^{13}C$ in CO_2 (bottom: University of Colorado, INSTAAR, courtesy James White) from weekly samples at Cape Kumukahi, HI.

After a decade of near-zero growth, atmospheric methane increased globally in 2007 by 7.5 ppb (Rigby et al. 2008), driven by increased Arctic and tropical emissions. Likely causes were anomalously high temperatures and precipitation in wetland regions, particularly in the Arctic: CO measurements indicated little contribution from enhanced biomass burning. In 2008, globally averaged atmospheric CH_4 increased again, with most of the increase driven by the tropics. Arctic emissions returned to normal despite continued warmth. The 2007–08 La Niña, with excess precipitation in Indonesia and parts of Amazonia (Plate 2.1, panel 6) , may be responsible for increased tropical emissions, but the current atmospheric CH_4 observing network, including in situ and remotely sensed observations, is insufficient to determine with certainty the causes of the CH_4 increases in 2007 and 2008.

(c) Carbon monoxide

Carbon monoxide does not strongly absorb terrestrial infrared radiation, but it impacts climate

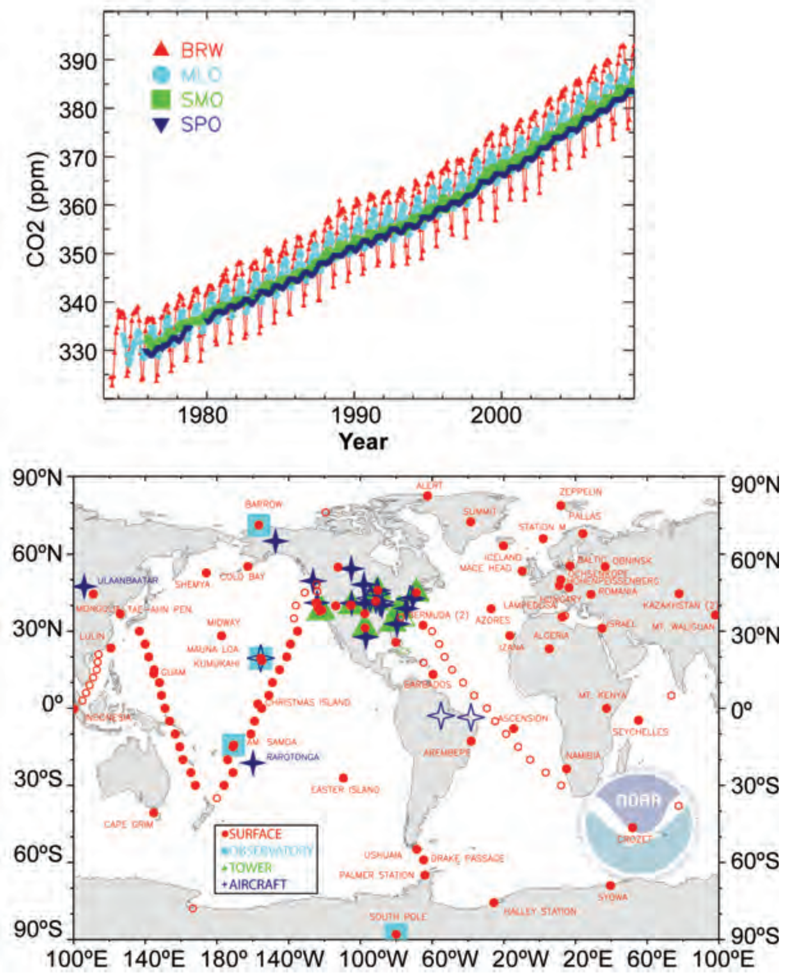

Fig. 2.28. (a) CO_2 monthly mean mole fractions determined from NOAA ESRL observatories at Barrow, AK; Mauna Loa, HI; American Samoa; and South Pole, part of the larger global carbon-cycle monitoring network shown in (b). 2008 results are preliminary. Data are courtesy of Kirk Thoning, NOAA ESRL. Current CO_2 trends at MLO are available at www.esrl.noaa.gov/gmd/ccgg/trends/. Additional plots can be found at www.esrl.noaa.gov/gmd/ccgg/iadv/ and www.esrl.noaa.gov/gmd/Photo_Gallery/GMD_Figures/ccgg_figures/.

through its chemistry. This affects OH (which influences the lifetimes of CH_4 and HFCs) and tropospheric O_3 (itself a greenhouse gas), so emissions of CO can be considered equivalent to emissions of CH_4 (Prather 1996). Current emissions of CO may contribute more to radiative forcing over decadal time scales than emissions of anthropogenic N_2O (Daniel and Solomon 1998).

There has been no long-term CO trend since ESRL measurements began in 1990 (Novelli et al. 2003), but CO enhancements occurred during 1997 to 1998, and again in 2002 to 2003. These are likely the result of tropical (Langenfelds et al. 2002) and boreal biomass burning (Kasischke et al. 2000). Because the lifetime of CO is only a few months, the CO enhancements quickly disappeared.

The preliminary globally averaged CO mole fraction in 2008 of 83 ppb is 12 ppb lower than in 1998 when there was a large contribution from biomass burning. ESRL's surface sampling network is less sensitive to biomass-burning emissions of CO than remotely sensed CO observations such as MOPITT (Pan et al. 1998), because emissions are rapidly transported away from the surface where the sampling sites are located. The combination of surface measurements and MOPITT retrievals may improve our understanding of the contribution of biomass burning to atmospheric CH_4.

(ii) Ozone-depleting gases and their replacements—S. A. Montzka

Long-lived halocarbons affect the radiative balance of the atmosphere because they efficiently absorb terrestrial IR radiation (see next section). Long-lived halocarbons containing bromine and chlorine also influence the radiative atmospheric balance indirectly through their destruction of stratospheric ozone. So production of many halocarbons has been restricted following the 1987 Montreal Protocol on Substances that Deplete the Ozone Layer. As a result, mixing ratios of most of the potent ozone-depleting gases have been declining at Earth's surface; this decline continued in 2008 (Fig. 2.29).

The mixing ratios of some halogenated gases continue to increase globally (Fig. 2.29). The most rapid increases are observed for HCFCs and HFCs, which are common replacements for CFCs, halons, and other ozone-depleting gases. Increases in HCFCs have recently accelerated because of enhanced use in developing countries (Montzka et al. 2009). Both HCFCs and HFCs are efficient absorbers of infrared radiation (Table 2.4). Although HCFCs contain chlorine and deplete ozone with a reduced efficiency compared to CFCs, HFCs do not participate in ozone-destroying reactions.

The influence of halocarbon trace-gas trends on future levels of stratospheric ozone can be estimated from weighted sums of Cl and Br in long-lived halocarbons provided that the enhanced efficiency for Br to destroy ozone is considered [a factor of 60 is used here (Clerbaux and Cunnold et al. 2007)]. For midlatitudes this sum is expressed as EECl (Fig. 2.29) and is derived from surface-based measurements. It provides an estimate of the near-future ozone-depleting power of trace gases, when air at Earth's surface will have become mixed into the midlatitude stratosphere. A second metric, ECl, provides an estimate of the ozone-depleting power of trace gases in the near future for the stratosphere over the polar regions.

The EECl content of the lower atmosphere has declined fairly steadily since the peak in 1994 at a mean rate of 28 parts per trillion yr^{-1}. Despite these substantial changes, full recovery of stratospheric ozone is not expected until the mid- to late-twenty-first century due to the long lifetime of many of these chemicals [Fig. 2.29 (bottom); Table 2.4]. Progress toward EECl reductions can now be readily assessed with the NOAA ODGI (see www.cmdl.noaa.gov/odgi/; Hofmann and Montzka 2009), which is derived from EECl. It is scaled so that a value of 100 represents the EECl abundance at its peak, and 0 represents the 1980 level (when ozone depletion was thought to have been small). In 2008 the ODGI–Midlatitudes was 70.8 (Fig. 2.29). Less progress is evident in ECl; the ODGI-Antarctica derived from ECl estimates was 84.5 in 2008.

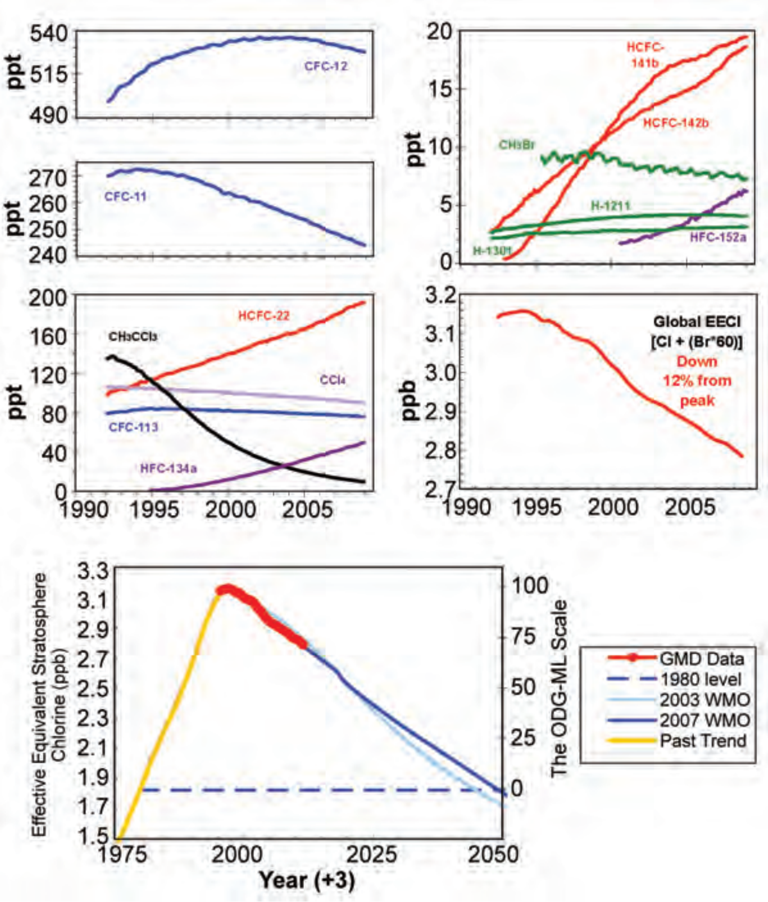

Fig. 2.29. Changes in global mean tropospheric mixing ratios (ppt, or pmol mol^{-1}) of the most abundant CFCs, HCFCs, HFCs, chlorinated solvents, and brominated gases. The middle right-hand panel shows secular changes in atmospheric equivalent chlorine (EECl; ppb or nmol mol^{-1}), which is an estimate of the ozone-depleting power of these atmospheric halocarbons. EECl is derived from observed mixing ratios of ozone-depleting gases appearing in the other four panels, and it is derived from the sum of [Cl + (Br×60)] contained in these gases. The bottom shows the recent changes in EESC observed by the NOAA/GMD global network relative to the secular changes observed in the past, including the level observed in 1980 when the ozone hole was first observed, and a projected future. The Ozone Depleting Gas Index for midlatitudes is derived (right-hand axis) from rescaling EESC. EESC is derived from EECl by simply adding 3 yr to the time axis to represent the lag associated with mixing air from the troposphere to the middle stratosphere, where the ozone layer resides [Source: Montzka et al. (1996, 1999.)]

(iii) The combined influence of long-lived trace gases on the radiative balance of the atmosphere—S. A. Montzka

The direct radiative influence of a trace gas is directly proportional to its atmospheric abundance and how efficiently it absorbs infrared radiation in specific regions of the electromagnetic radiation spectrum (its radiative efficiency; Table 2.4). High-precision measurements of CO_2, CH_4, N_2O, CFC-12, CFC-11 (the major long-lived greenhouse gases) and 10 minor greenhouse gases (CFC-113, HCFCs, HFCs, etc., see Table 2.4 for complete list) from the NOAA global air sampling network have been used to calculate the overall change in the direct radiative climate forcing (Hofmann et al. 2006) (Fig. 2.30). This is calculated from changes in the abundances of these gases since 1750, and by mid-2007 amounted to approximately 2.69 W m^{-2}, of which changes in the abundance of CO_2 accounted for 63%.

TABLE 2.4. Radiative efficiencies and lifetimes of chemicals considered in the AGGI and OGDI.

Industrial Designation or Common Name	Chemical Formula	AGGI	ODGI	Radiative Efficiency (W m^{-2} $ppbv^{-1}$) *	Mixing ratio [change from 2006 to 2007]**	Lifetime
Carbon Dioxide	CO_2	Y	N	$1.41\text{x}10^{-5}$	382.6[1.7]	
Methane	CH_4	Y	N	$3.7\text{x}10^{-4}$	1781.4[6.0]	12.0
Nitrous oxide	N_2O	Y	N	$3.03\text{x}10^{-3}$	321.9[0.7]	114
Chlorofluorocarbons						
CFC-11	CCl_3F	Y	Y	0.25	247.3[−2.3]	45
CFC-12	CCl_2F_2	Y	Y	0.32	530.6[−1.8]	100
CFC-113	CCl_2FCClF_2	Y	Y	0.30	77.4[−0.8]	85
Hydrochlorofluorocarbons						
HCFC-22	$CHClF_2$	Y	Y	0.20	182.9[7.7]	12.0
HCFC-141b	CH_3CCl2F	Y	Y	0.14	18.7[0.6]	9.3
HCFC-142b	CH_3CClF_2	Y	Y	0.20	17.2[1.2]	17.9
Hydrofluorocarbons						
HFC-134a	CH_2FCF_3	Y	N	0.16	43.2[4.3]	14
HFC-152a	CH_3CHF_2	N	N	0.09	5.3[0.7]	1.4
Chlorocarbons						
Methyl Chloroform	CH_3CCl_3	Y	Y	0.06	12.9[−2.5]	5.0
Carbon Tetrachloride	CCl_4	Y	Y	0.13	92.1[−1.2]	26
Methyl Chloride	CH_3Cl	N	Y	0.01	548[7.3]	1.0
Bromocarbons						
Methyl Bromide	CH_3Br	N	Y	0.01	7.6[0.0]	0.7
Halon 1211	$CBrClF_2$	Y	Y	0.30	4.1[−0.03]	16.0
Halon 1301	$CBrF_3$	Y	Y	0.32	3.1[0.03]	65
Halon 2402	$CBrF_2CBrF$	N	Y	0.33	0.47[−0.01]	20
Fully fluorinated species						
Sulfur Hexafluoride	SF_6	Y	N	0.52	6.16[0.26]	3,200

* Radiative forcings and lifetimes are taken from Daniel and Velders et al. (2007) and Clerbaux and Cunnold et al. (2007).

** Mixing ratios are measured global surface means determined from NOAA global cooperative sampling network (Hofmann et al. 2006). Changes indicated in brackets are simply the difference between the 2007 and 2006 annual global surface mean mixing ratios. Units are ppm for CO_2, ppb for CH_4 and N_2O, and ppt for all others.

The NOAA AGGI is based on the direct radiative forcing calculated from these NOAA measurements (Hofmann et al. 2006). It is calculated as a ratio relative to the direct radiative forcing calculated from these gases for 1990, the Kyoto Protocol baseline year; indirect effects (e.g., arising from ozone depletion or water-vapor feedbacks) are not considered. By 2007, the AGGI was 1.241 (Fig. 2.30). Increases in the atmospheric abundance of CO_2 accounted for 80% of the increase since 1990.

(iv) Nitrous oxide and sulfur hexafluoride—J. W. Elkins and G. S. Dutton

Nitrous oxide (N_2O) and sulfur hexafluoride (SF_6) are important atmospheric trace gases. Atmospheric N_2O has the third-strongest radiative forcing since

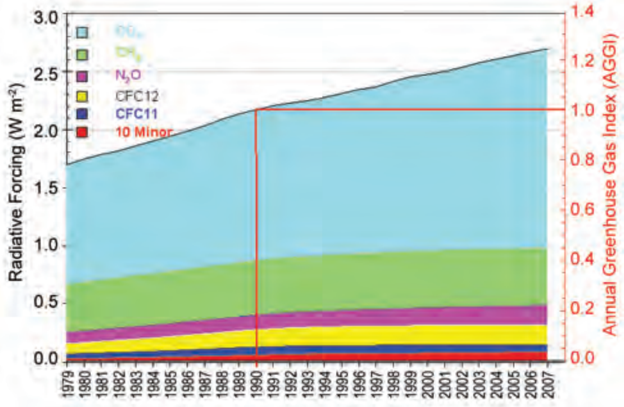

FIG. 2.30. The NOAA AGGI shows radiative forcing relative to 1750, of all the long-lived greenhouse gases indexed to 1 for the year 1990. Since 1990, radiative forcing from greenhouse gases has increased 24%.

the beginning of the Industrial Revolution after carbon dioxide and methane, while SF_6 represents the fourth-strongest forcing (Table 2.4). Atmospheric N_2O is also a source of stratospheric nitric oxide that is involved in stratospheric ozone depletion, and 30% of its sources are man made (fertilizers, industrial by-products, human and animal waste, and catalytic converters). SF_6 is 100% man made; it is used primarily for insulation in the distribution of electric power. Nitrous oxide has been growing since 1978 at a relatively constant growth rate of 0.772 ppb yr^{-1} with important biennial oscillations in its growth rate resulting from atmospheric transport (Fig. 2.31). Sulfur hexafluoride's growth rate has been increasing since 2003; note the recent deviation from a linear growth rate of 0.223 ppt yr^{-1} over 11 yr in Fig. 2.31, due to the world's growing demand for electricity.

2) GLOBAL AEROSOLS—J. Haywood, N. Bellouin, and A. Jones

Aerosols impact climate by scattering and absorbing solar and terrestrial radiation (direct effects) and by influencing the microphysical and optical properties of clouds, thereby influencing cloud development (indirect effects). The effects of anthropogenic aerosols remain major uncertainties in driving climate change. The global distribution of aerosols in 2008 was generally in line with that from climatology and with that from 2007 as demonstrated by aerosol optical depths derived from the MODIS sensor on the *Aqua* platform (Fig. 2.32). Except for the biomass-burning plume over the rain forests of Brazil in 2007 and the increased aerosol optical depths over northeastern Eurasia in 2008, the global distributions (and the global means) are very similar.

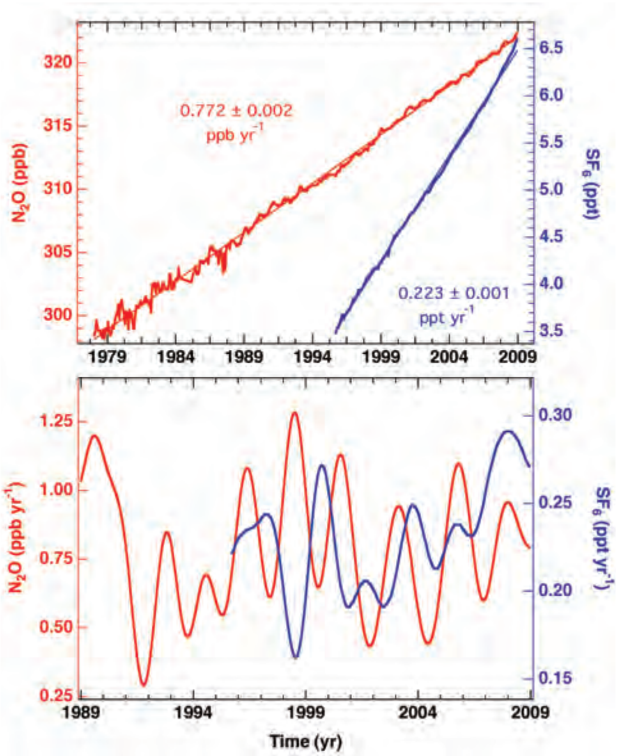

FIG. 2.31. (top) Global monthly means along with estimates for the linear growth rate of atmospheric nitrous oxide (N_2O, red) in ppb and sulfur hexafluoride (SF_6, blue) in ppt from the NOAA/ESRL halocarbon network. (bottom) Instantaneous growth rate of N_2O and SF_6 using a smoothing algorithm with a 2-yr filter; note the rapid rise of the atmospheric SF_6 growth rate after 2003. Atmospheric data for N_2O prior to 1989 and for SF_6 prior to 1999 were analyzed from flasks instead of continuously operating instruments at NOAA/ESRL baseline observatories.

The reduced Amazonian optical depth in 2008 is more in line with anomalously clear skies also noted in 2006 (Koren et al. 2007), than with the increasing trend seen from 2000 to 2007 (Evan 2007). Increased aerosol optical depths over northeastern Eurasia appear to arise from intense, large-scale boreal forest fires during April and July 2008. The number of acres burned by wildfires in the United States was significantly less (5.2 million) than the peak in 2006 (9.9 million).

Aerosol algorithm development continues apace with many improved products since the early ocean-only 2-channel retrievals of AVHRR (e.g., Mishchenko et al. 2007). Algorithms can now determine the fine-mode fraction of aerosols (e.g., MODIS; Remer et al. 2005) and speciated aerosol optical depths (e.g., MISR; Kahn et al. 2005). The use of multisensor algorithms allows estimation of the anthropogenic aerosol optical depth, which is important in determining the radiative forcing of aerosols (Forster et al. 2007) as well as any anthropogenically influenced trend. Figure 2.32c shows the anthropogenic aerosol optical depth determined from MODIS using the retrieval algorithm of Bellouin et al. (2008). The anthropogenic aerosol optical depth consists primarily of industrial pollution (mainly sulfate, nitrate, organic carbon, and black carbon) and biomass-burning smoke (mainly volatile organic carbon, black carbon, and inorganic compounds). It averages around 0.03 over the ocean but exceeds 0.1 over many land areas.

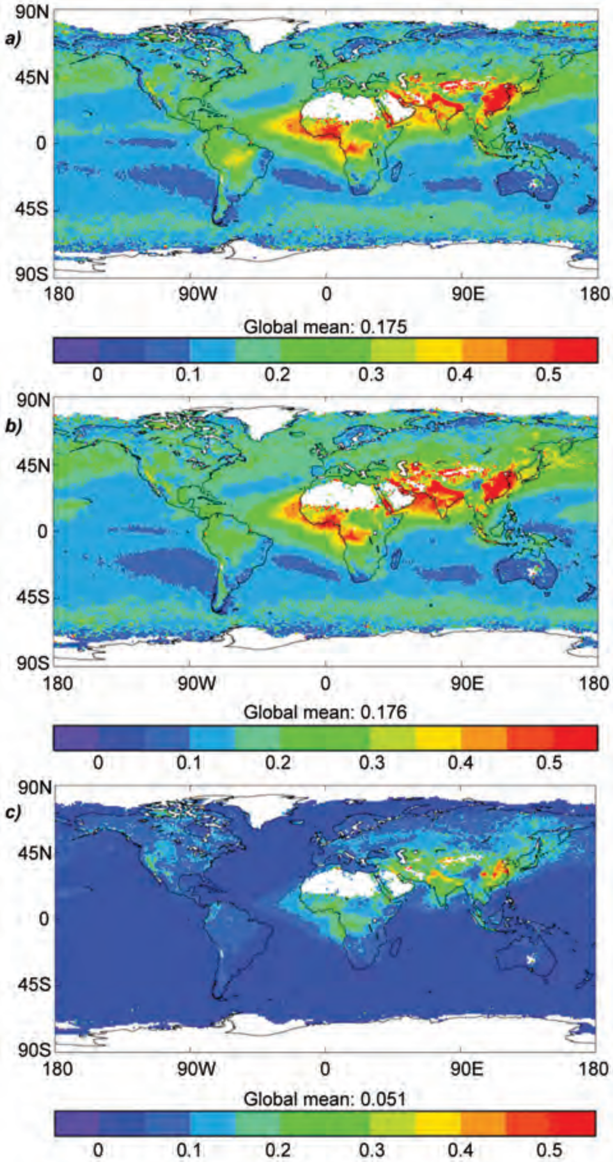

Fig. 2.32. Annual mean total aerosol optical depth derived from the MODIS *Aqua* sensor for (a) 2007, (b) 2008. (c) The anthropogenic aerosol optical depth derived from MODIS aerosol optical depths and fine-mode fractions for 2008, following Bellouin et al. (2008). Missing data areas are white.

Decreases (increases) in sulfur dioxide emissions over Europe and eastern Asia continue to be linked to increases (decreases) in surface solar radiation leading to brightening (dimming) (e.g., Wild et al. 2005). These dimming/brightening features are explicitly modeled in climate scenarios by including the effects of aerosol on radiation as shown in Fig. 2.33. Over Europe the brightening since the mid-1980s evident in the observations and in the modeling shown in Fig. 2.33 also appears well correlated with changes in atmospheric visibility (e.g., Vautard et al. 2009). The analysis of visibility trends attributes some, but not all, of the recent warming trend in the region to this phenomenon.

3) Stratospheric ozone—M. Weber

The Antarctic ozone hole area with total column ozone below 220 DU reached a maximum of 26 million km^2 by the end of September 2008; among the largest on record (www.temis.nl/protocols/o3hole/data/fd-o3area220.pdf). October total ozone above Antarctica and the tip of South America was up to 30 DU below the long-term mean. The annual anomaly was negative for most parts of the globe except for a narrow band in the tropics and a small region near the North Pole with positive anomalies of up to 10 DU (Plate 2.1, panel 9). Large negative annual anomalies were observed above Russia due to a shift of the Arctic polar vortex into this region during spring as well as lower ozone during fall. The positive tropical anomaly is related to the QBO (Baldwin et al. 2001), which was mainly in the west phase near 50 hPa. The QBO signal as well as the 11-yr solar cycle signature in the tropics is clearly evident in the total ozone anomaly time series (Fig. 2.34).

The long-term evolution of total ozone (Fig. 2.34) is dominated by lower stratospheric ozone (~30–100 hPa or 15–25 km) and can be divided into two phases. A steady decline at mid- to high latitudes from satellite record inception lasted until about the mid-1990s, followed by a sharp increase, then leveling off in recent years in the Northern Hemisphere and a leveling off with some enhanced interannual variability in the Southern Hemisphere (Fig. 2.35). Important factors are the 11-yr solar cycle, major volcanic eruptions, the QBO, and chemical ozone loss (Staehelin et al. 2001). The total ozone changes since the mid-1990s can be attributed in part to changes in the halogen load [section 2f1(iv); Dhomse et al. 2006; Froidevaux et al. 2006; Newman et al. 2006, 2007; Stolarski and Frith 2006; Yang et al. 2005]. However, changes in stratospheric circulation pattern and atmospheric dynamics, for example, Brewer–Dobson

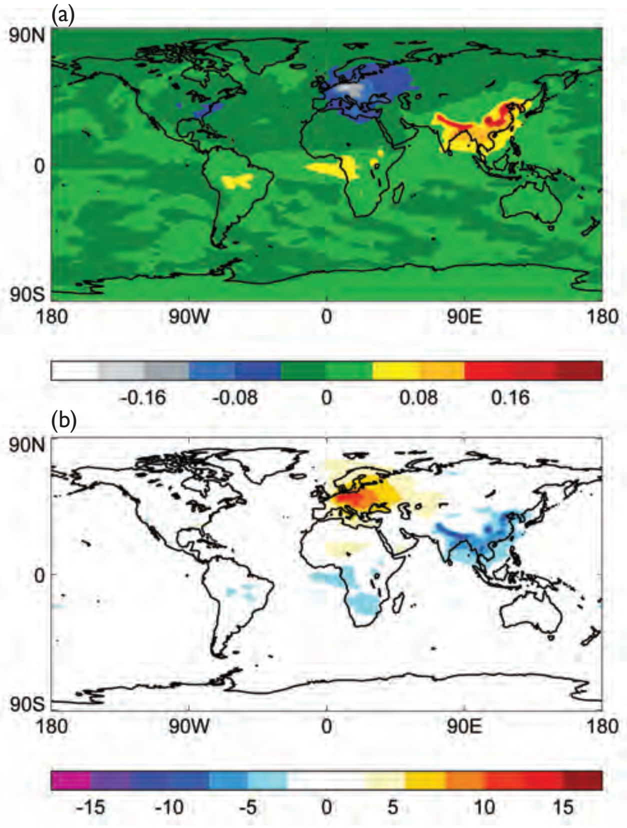

Fig. 2.33. (a) The change in aerosol optical depth simulated by the Met Office HadGEM1 over the period 1980 to 2000. Blue and gray represent a decrease in aerosol optical depths over Europe and the eastern United States due to more stringent emission controls, while red and yellow represent emissions from increasingly industrialized regions. (b) The modeled change in sunlight received at the surface (W m^{-2}) for the same period—"brightening" is shown in yellow/orange, while "dimming" is shown in the blue colors.

circulation (Weber et al. 2003; Dhomse et al. 2006), teleconnection patterns such as the North Atlantic Oscillation (Appenzeller et al. 2000; Orsolini et al. 2004), and atmospheric advection (Wohltmann et al. 2007), all contribute to winter ozone transport from the tropical production region into middle and high latitudes and explain the large observed interannual variability in extratropical ozone (Fig. 2.35). A record-high chemical ozone loss in Arctic winter 2004/05 (Rex et al. 2006; Newman and Rex 2007) and record-size ozone hole above Antarctica in 2006 indicate that stratospheric halogen load still remains high. The rate of recovery in coming decades will strongly depend on the influence of climate change on stratospheric circulation and temperatures in addition to the expected decrease in ozone-depleting substances (Waugh et al. 2009).

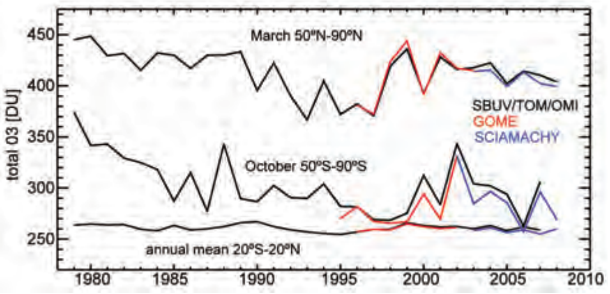

Fig. 2.34. Time series of SBUV/TOMS/OMI (black), GOME (red), and SCIAMACHY (blue) total ozone in the bands 50°–90°N in Mar, 20°S–20°N (annual mean), and 50°–90°S in Oct. Anomalies were calculated from area-weighted monthly mean zonal mean data in 5° latitude steps by removing the seasonal mean from the period 1979–89.

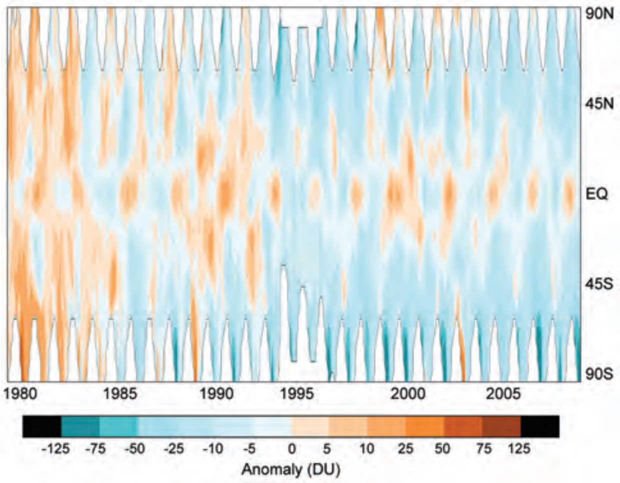

Fig. 2.35. Time variation (1979–2008) of zonally averaged total ozone anomalies. Anomalies are based on the merged SBUV/TOMS/OMI up to Jun 1995 (Frith et al. 2004), GOME from Jul 1995 to May 2003, and SCIAMACHY data from Jun 2003 to Dec 2008 (Weber et al. 2007).

The upper stratosphere is a more favorable region to investigate ozone recovery because long-term changes are larger than observed in column ozone and atmospheric dynamics are less influential (Newchurch et al. 2003). By the end of the 1990s ozone near 40-km altitude had decreased by ~8% decade^{-1} at middle latitudes and then leveled off after that or slightly increased, in agreement with changes in the halogen load (Steinbrecht et al. 2009; Jones et al. 2009). In this region an eventual "super recovery" (Newman and Rex 2007) to ozone levels greater than 1960 levels can be expected if stratospheric temperatures continue to cool (Eyring et al. 2006). Surprisingly, there are indications that upper stratospheric temperatures near 40-km altitude have not changed significantly over the past 20 yr (Steinbrecht et al. 2009), though temperature trends in this altitude region are not consistent among different datasets (section 2b3).

g. *Land surface properties*

1) Alpine glaciers and ice sheets—M. S. Pelto

The WGMS (WGMS 2007, 2008) provides annual global indices based on alpine glacier mass balance and terminus position, as these reflect annual volume change (Oerlemans 1994). However, a 9-month time lag prevents immediate assessment of the global state of alpine glaciers in 2008.

Worldwide retreat of mountain glaciers is one of the clearest signals of climate change (Haeberli and Hoelzel 1995). It reflects strongly negative mass balances over the last 30 yr (WGMS 2007). Mass balance is the most appropriate climate parameter for glaciers because it is an annual integral of local weather conditions (Pelto and Hedlund 2001). The change in glacier length is a smoothed and delayed response to the mass balance changes (Haeberli and Hoelzle 1995). The recent rapid retreat and prolonged negative balances have led to some glaciers disappearing (Pelto 2006).

Glacier mass balance is the difference between accumulation and ablation. Variations in temperature and/or snowfall alter the mass balance. A glacier with a sustained negative (positive) balance will retreat (advance) to reestablish equilibrium by decreasing (increasing) the area at lower elevations where ablation is highest. If a glacier lacks a consistent accumulation zone, it is in disequilibrium with climate and will disappear (Pelto 2006; Paul et al. 2007).

In 2007 the mean mass balance of all the WGMS reporting glaciers was −528-mm water equivalent; it was −673 mm for 30 reference glaciers with 30 yr of record, the 17th consecutive year of negative mass balance (Fig. 2.36a). A loss of 0.9 m of water equivalent is the same as the loss of 1.0 m of glacier thickness, since ice is less dense than water. The trend demonstrates why alpine glaciers are currently retreating. The cumulative loss of the last 30 yr (Fig. 2.36b) is the equivalent of cutting a 12–14-m-thick slice off of the average glacier. The trend is remarkably consistent from region to region (WGMS 2007), and the results from the 30 reference glaciers are not appreciably different from those for all monitored glaciers (Fig. 2.36b).

The WGMS glacier terminus position data overemphasize the European Alps, but the overall global and regional records are very similar, except for New Zealand. The proportion of advances in Europe, Asia, and North America reached a minimum in 2005 when of 442 glaciers examined, 26 advanced, 18 were stationary, and 398 (90%) retreated. Overall there has been a substantial volume loss of 11% of New Zealand glaciers from 1975 to 2005 (Salinger NWIA).

In 2008 New Zealand snowlines were 130 m above the elevation for equilibrium leading to negative mass balances and a new record minimum total ice volume for the southern Alps since records began in 1976. In Switzerland negative balances ranged from −0.6 to −1.6 m, and of the 80 glacier termini reporting to date 73 were retreating, 2 advancing, and 5 stationary (Bauder, VAW/ETH). In Norway, of 32 glaciers observed in 2008, 24 retreated, 3 advanced, and 5 were stationary (H. Elvehoi, NVE). The Pacific Northwest of North America experienced strong La Niña conditions with extra snowfall, so mass balances of North Cascade and southeast Alaska glaciers were positive in 2008.

In northern Greenland, ice melt in 2008 lasted 18 days longer than the previous maximum and the melt

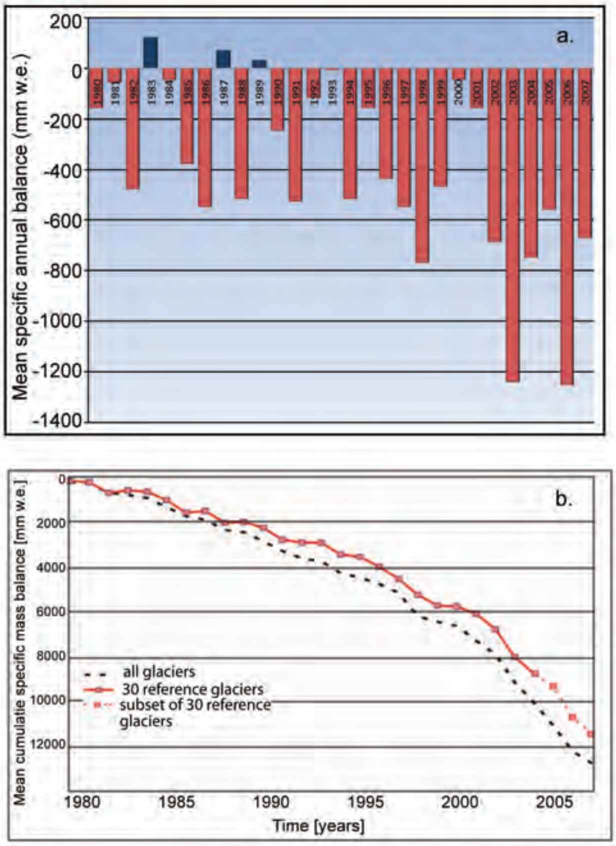

Fig. 2.36. (a) The mean annual mass balance (mm water equivalent) of 30 WGMS reference glaciers, 1980–2007. (b) The mean cumulative mass balance for the 30 reference glaciers and all monitored glaciers. The dashed line is for subset of 30 reference glaciers because not all 30 glaciers have final data for the last few years.

index was 300% of the 1979–2007 average (Tedesco et al. 2008). The record ablation in northern Greenland reflected regional warmth that led to the breakup of 29 km^2 of the floating terminus lobe of Petermann Glacier (Box and Howat, Ohio State), as well as the breakup of Arctic ice shelves on the north coast of Ellesmere Island. Ward Hunt lost 22 km^2, Serson Ice Shelf lost 122 km^2—60% of its area—and Markham lost all 50km^2 of its area (Muller, Trent University).

In Antarctica, Wilkins ice shelf lost 400 km^2 in a rapid February collapse. Humbert and Braun (2008) noted that ongoing thinning had preconditioned it for collapse and that existing rifts in February 2008 suggested that an additional 2000 km^2 was in imminent danger of collapse. During the austral winter an additional 1350 km^2 was lost.

2) Land cover—A. S. Belward, E. Bartholomé, F. Achard, and A. B. Brink

We have begun to make significant progress in documenting the climate-forcing effects of land cover, through increasingly accurate mapping of the global distribution of land-cover types and ongoing changes. At the turn of the millennium a quarter of the land surface was unvegetated (barren, permanent snow and ice, or urban), 30% was grass and shrubland, 29% was forest, and the remaining 16% was devoted to agriculture (Bartholomé and Belward 2005; Fig. 2.37).

In 2008 the U.S. Geological Survey made the Landsat archives—which extend back to 1972—freely available. These data are being used to measure rates and patterns of land cover change, first on a continental and pan-tropical scale, and eventually glob-

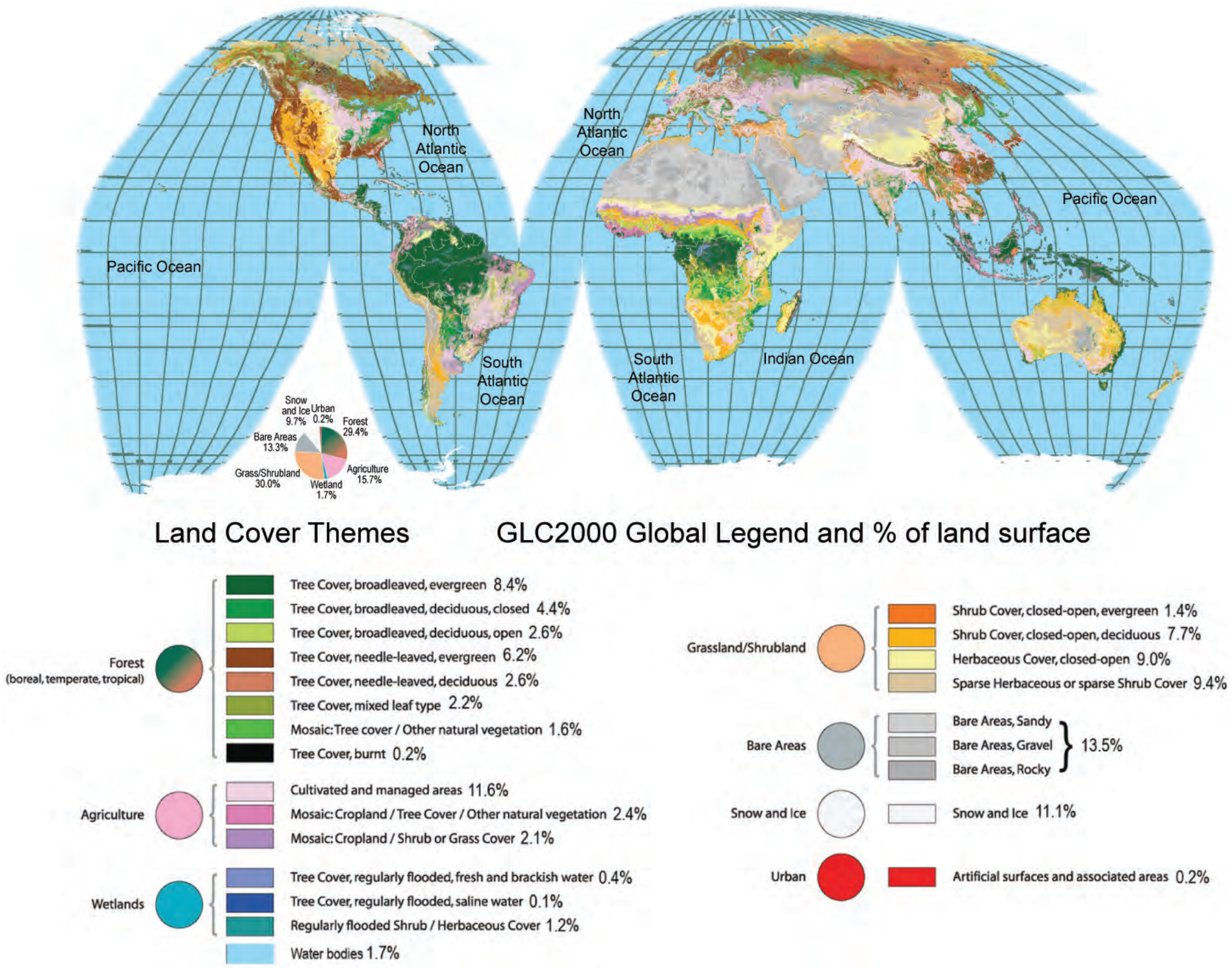

Fig. 2.37. Global land cover at the turn of the millennium: 22 land-cover classes, legend compatible with the FAO Land Cover Classification System (Di Gregorio and Jansen 2000). Projection Interrupted Goode Homolosine Classification derived from daily SPOT VGT satellite observations, 1 × 1 km grid cell, between Nov 1999 and Dec 2000. Map and independent reference data agree 68.6% of the time (Mayaux et al. 2006). Twenty-two percent of the misclassified areas occur in the mixed classes (e.g., some areas known from reference data to be broad-leaved deciduous forest have been mapped as mixed forest).

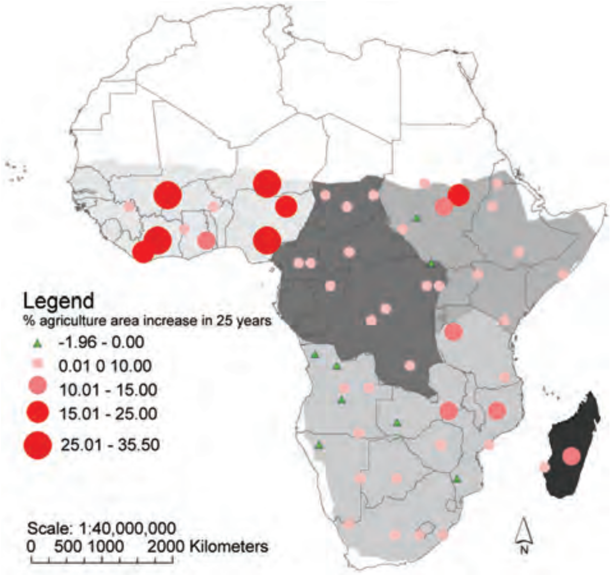

Fig. 2.38. Conversion of natural vegetation to agriculture and reversion of agriculture to natural vegetation between 1975 and 2000 for Africa; rates range from −1.96% to 35.5%

ally. Results for Africa, shown in Fig. 2.38, indicate that since 1975 around 5 million hectares of Africa's natural vegetation have been converted to agriculture each year. This affects albedo, roughness, evapotranspiration, carbon exchange, and aerosol emissions on a continental scale, though the magnitude of the effects relative to natural variability and other external forcing influences has yet to be determined. "Hotspots" of savanna clearance in West Africa are particularly evident, as are the low rates of change in the African humid forest biome (Brink and Eva 2008).

Using a combination of Landsat and MODIS data, Hansen et al. (2008) estimated humid tropical forest clearance between 2000 and 2005 to be 27.2 million hectares or a 2.36% reduction in area. Forest clearing is highly localized, with 55% of the loss being concentrated in just 6% of the humid tropical forest biome—mostly in Latin America and southeast Asia. The Americas lost 2.56% of their humid tropical forest between 2000 and 2005 and Asia lost 2.9%, while Africa lost less than 0.8%.

The ESA has released new global land cover data for 2005, based on MERIS observations and with a spatial resolution of 300 m (Arino et al. 2008). NASA has released for evaluation a new global land cover dataset for 2001–05 based on MODIS observations at a spatial resolution of 500 m (Strahler et al. 1999). These datasets will form a basis for extending cover-change analysis beyond Africa and the tropics and are evidence of renewed attention to land cover by space agencies. The changes in global land cover reported here are anthropogenic in origin, driven by the increasing need of our growing population for land to supply food, fuel, fiber, and shelter. Land cover is also in part determined by regional climate, and as climates change so too does the distribution of vegetation, barren land, water bodies, snow, and ice. Population growth—and climate change—makes future changes in land cover inevitable.

3) Global vegetation condition—N. Gobron and A. S. Belward

The Fraction of Absorbed Photosynthetically Active Radiation is crucial for the energy and carbon balances of ecosystems. It can be used in quantifying CO_2 assimilation by plants and the release of water through evapotranspiration. Daily observations of FAPAR provide a basis for monitoring the seasonal cycle and long-term trends of vegetation, and the data have been used in diagnostic models, for example, to examine the role of the terrestrial biosphere in climate-carbon feedbacks (Knorr et al. 2007).

Rates of photosynthesis are affected by temperature and precipitation, so favorable temperatures and soil moisture availability (extreme heat and/or drought) are accompanied by higher- (lower-) than-average FAPAR. Other influences on plant physiology and plant health, such as pollution, disease, insect attack, wind-throw, and fire, also affect FAPAR. Such perturbations tend to be episodic, though the savanna fires of Africa, for example, are a yearly feature.

Since 1998 FAPAR has been derived from a range of polar-orbiting platforms (Knyazikhin et al. 1998;

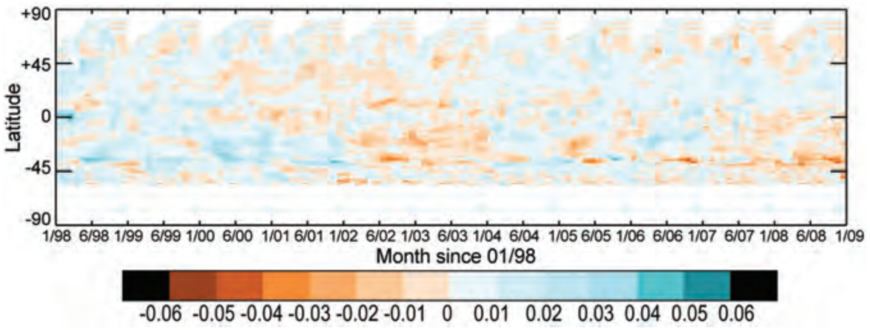

Fig. 2.39. Zonal-average FAPAR anomalies 1998–2008. Values range from −0.06 to 0.06.

Gobron et al. 2006, 2008). Figure 2.39 is derived from SeaWiFS (NASA 1998 to 2006) and MERIS (ESA 2002 to 2008), both of which have been subject to rigorous comparison with reference data (Gobron et al. 2006, 2008). Global vegetation dynamics, as represented by FAPAR, show considerable interannual variations. The Southern Hemisphere generally shows more variability than the Northern Hemisphere, reflecting the greater impact of ENSO events on vegetation at these latitudes. The Northern Hemisphere shows the impacts of the major heat waves of 2003 (Europe) and 2007 (western and central Russia). In 2008 (Plate 2.1, panel 10) the strongest negative anomaly reflected severe drought in Argentina's steppe and grassland. Southeastern Amazonia had negative anomalies, arising partly from intense land-use transformations (Malhi et al. 2008). There were also major negative anomalies in Australia and central Asia. In contrast, much of China, southern Africa's savannas, and northern high latitudes enjoyed better-than-average vegetation vigor in 2008.

FAPAR products (Fig. 2.39), along with reprocessed historical archives and planned missions, have the potential to greatly improve our understanding of vegetation–climate interactions.

TABLE 2.5. Sources of those datasets used in this chapter that are publicly available for bona fide research purposes.

Source	Datasets
http://www.hadobs.org	HadCRUT3 (surface temperatures), HadAT (radiosonde temperatures), HadSLP2r (SLP and derived indices)[a]
http://www.ncdc.noaa.gov/oa/climate/research/anomalies/anomalies.html	NCDC (surface temperatures)
http://data.giss.nasa.gov/gistemp/	GISS (surface temperatures)
http://www.ncdc.noaa.gov/oa/climate/ratpac/index.php	RATPAC (radiosonde temperatures)
http://earth.geology.yale.edu/~sherwood/radproj/	IUK (radiosonde temperatures)[b]
http://www.univie.ac.at/theoret-met/research/raobcore/	RAOBCORE and RICH (radiosonde temperatures)
http://vortex.nsstc.uah.edu/data/msu/	UAH MSU record (satellite temperatures)
http://www.remss.com	RSS MSU record (satellite temperatures), RSS SSM/I record (winds, precipitation and TCWV over the oceans), TMI and AMSR-E (precipitation)[c]
http://www.star.nesdis.noaa.gov/smcd/emb/mscat/mscatmain.htm	STAR MSU record (satellite temperatures)
On request from junhong@ucar.edu	Land-based GPS TCWV
http://www.geo.unizh.ch/wgms/mbb/mbb10/sum07.html	Glacial Mass Balance data
http://gem.jrc.ec.europa.eu/index.php	Global land cover[a]
http://www.ncdc.noaa.gov/oa/climate/ghcn-monthly/index.php	GHCN monthly (precipitation)[d]
http://www.ncdc.noaa.gov/oa/climate/ghcn-daily/	GHCN daily[d]
http://www.cdc.noaa.gov/data/gridded/data.gpcc.html	GPCC (VasClimO and Full v.3) (precipitation)
http://precip.gsfc.nasa.gov	GPCP (precipitation)
http://www.cpc.noaa.gov/products/global_precip/html/wpage.cmap.html	CMAP (precipitation)
http://climate.rutgers.edu/snowcover	Snowcover extent
http://www.atmos.washington.edu/~ignatius/CloudMap	SOBS cloud
http://www.ssec.wisc.edu/~donw/PAGE/CLIMATE.HTM	HIRS-W cloud
http://isccp.giss.nasa.gov	ISCCP D2 cloud
http://cimss.ssec.wisc.edu/patmosx	PATMOS-x cloud
http://ladsweb.nascom.nasa.gov	MODIS cloud
http://www.cdc.noaa.gov/data/reanalysis	NCEP–NCAR reanalysis
http://www.gth-h.net	Runoff data
http://eosweb.larc.nasa.gov/	CERES EBAF, CERES ERBE-like, and FLASHFlux data (satellite broadband earth radiation budget; outgoing longwave, reflected shortwave, and net radiation)[e]
http://www.esrl.noaa.gov/gmd/aggi/	Greenhouse gas index
http://www.esrl.noaa.gov/gmd/ccgg/trends/	Carbon dioxide monitoring
www.esrl.noaa.gov/gmd/ccgg/towers/	ESRL carbon monoxide monitoring
http://www.cmdl.noaa.gov/odgi/	Ozone-depleting gas index
http://www.esrl.noaa.gov/gmd/dv/ftpdata.html	ESRL halocarbon network
http:// www.iup.uni-bremen.de/gome/wfdoas/	SBUV/TOMS/OMI, GOME, SCIAMACHY ozone
http://fapar.jrc.ec.europa.eu/	FAPAR

[a] Many additional land datasets available

[b] May move as site owner has changed institute

[c] Entire SSM/I record only available on hard disk.

[d] Also other variables

[e] Many additional datasets available; including clouds and aerosols